Spontaneous Seed Formation During Electrodeposition Drives Epitaxial Growth of Metastable Bismuth Selenide Microcrystals

Jiang Luo[1], Guodong Ren[2], Brandon M. Campbell[1], Dongyan Zhang[1], Tengfei Cao[3], Rohan Mishra[3,2]*, Bryce Sadtler[1,2]*

[1] Department of Chemistry, Washington University, St. Louis, Missouri 63130, United States

[2] Institute of Materials Science & Engineering, Washington University, St. Louis, Missouri 63130, United States

[3] Department of Mechanical Engineering & Materials Science, Washington University in St. Louis, St. Louis, Missouri 63130, United States

* To whom correspondence should be addressed. Email: rmishra@wustl.edu, sadtler@wustl.edu

Abstract

Materials with metastable phases can exhibit vastly different properties from their thermodynamically favored counterparts. Methods to synthesize metastable phases without the need for high-temperature or high-pressure conditions would facilitate their widespread use. We report on the electrochemical growth of microcrystals of bismuth selenide, Bi_2Se_3, in the metastable orthorhombic phase at room temperature in aqueous solution. Rather than direct epitaxy with the growth substrate, the spontaneous formation of a seed layer containing nanocrystals of cubic BiSe enforces the metastable phase. We first used single-crystal silicon substrates with a range of resistivities and different orientations to identify the conditions needed to produce the metastable phase. When the applied potential during electrochemical growth is positive of the reduction potential of Bi^{3+}, an initial, Bi-rich seed layer forms. Electron microscopy imaging and diffraction reveal that the seed layer consists of nanocrystals of cubic BiSe embedded within an amorphous matrix of Bi and Se. Using density-functional theory calculations, we show that epitaxial matching between cubic BiSe and orthorhombic Bi_2Se_3 can help stabilize the metastable orthorhombic phase over the thermodynamically stable rhombohedral phase. The spontaneous formation of the seed layer enables us to grow orthorhombic Bi_2Se_3 on a variety of substrates including single-crystal silicon with different orientations, polycrystalline fluorine-doped tin oxide, and polycrystalline gold. The ability to stabilize the metastable phase through room-temperature electrodeposition in aqueous solution without requiring a single-crystal substrate, broadens the range of applications for this semiconductor in optoelectronic and electrochemical devices.

Introduction

Many metastable materials exhibit promising catalytic, electronic, and optical properties, that make them attractive for applications in the conversion and storage of energy and information, including as electro- and photocatalysts for fuel generation,[1-4] electrodes for metal-air batteries,[5-6] and qubits for quantum computation.[7-8] Compared to their corresponding ground-state structures, metastable materials have a higher formation energy and are thus often difficult to synthesize under ambient conditions. For example, naturally occurring diamond forms at high pressures and temperatures. Innovations in the synthesis and doping of diamond via chemical vapor deposition[9-11] have enabled fundamental studies of nitrogen vacancies in this metastable material for applications in quantum sensing and computation.[7-8, 12]

Methods to synthesize metastable phases at moderate pressure and temperature include colloidal synthesis,[5, 13-14] chemical and physical vapor deposition,[6, 9-11] solid-state metathesis,[15-16] and electrodeposition.[3, 17-25] Electrodeposition is particularly attractive because it is a versatile and inexpensive method to produce metals,[3, 17-20] ceramics,[21, 26] and semiconductors[22-25, 27-36] at atmospheric pressure and temperatures below 100°C. Although many binary metallic alloys and intermetallic compounds with metastable structures have been prepared by electrodeposition,[3, 17-20] there only exist a few examples of electrodepositing metastable phases of semiconductor compounds including Bi_2Se_3,[23-25] CdSe,[22] and δ-Bi_2O_3.[21] To achieve high crystallinity during the electrodeposition of compounds with significant covalent bonding character, a single-crystal growth substrate is often required that provides epitaxial matching between the substrate surface (i.e., the working electrode of the electrochemical cell) and the structure of the desired phase. For example, both the zinc blende phase of CdSe (which is metastable relative to the wurtzite phase at room temperature) and the cubic δ phase of Bi_2O_3 (which is metastable relative to the monoclinic α

phase at room temperature) can be electrodeposited on single-crystal Au (111) substrates.[21-22] The requirement for a single-crystal substrate limits the scale up and commercial application of electrodeposition to achieve phase control and synthesize desirable metastable phases of ceramics and semiconductor compounds.[37]

Bismuth chalcogenides have been proposed as materials for photodetectors and photovoltaics,[23, 38-40] thermoelectrics,[41-44] and topological insulators.[45-46] The structures of bismuth chalcogenide compounds vary with the identity of the chalcogen atom. For example, the thermodynamically stable phase of Bi_2Se_3, which is isomorphic with Bi_2Te_3 and Sb_2Te_3, has a layered, rhombohedral crystal structure, as shown in **Figure 1a**. Rhombohedral Bi_2Se_3 with a narrow band gap of 0.35 eV has been proposed as a topological insulator.[45-46] The metastable phase of Bi_2Se_3 has an orthorhombic crystal structure, as shown in **Figure 1b**. Orthorhombic Bi_2Se_3 is isomorphic with Sb_2S_3 (i.e., stibnite), Sb_2Se_3, and Bi_2S_3; it consists of zigzagging chains of [$BiSe_5$] pyramids and distorted [$BiSe_6$] octahedra that share edges along the [001] direction. The optical band gap of 1.25 eV for orthorhombic Bi_2Se_3[23] combined with its strong absorption in the visible region and anisotropic crystal structure make this material of interest for optoelectronic devices including polarization-sensitive photodetectors.[38-39, 47-48]

Films of Bi_2Se_3 have previously been electrodeposited in both the rhombohedral and orthorhombic phases.[23-25, 44, 49-55] Electrodeposition on polycrystalline metal and metal oxide substrates (e.g., Au, Ru, Ti, Pt, stainless steel, or tin oxide) has produced films with the rhombohedral phase, a mixture of the two phases, or the orthorhombic phase with low crystallinity (i.e., films exhibiting small crystallite sizes and weak diffraction peaks).[25, 44, 50-55] Growth of phase-pure orthorhombic Bi_2Se_3 with high crystallinity has been reported only when electrodeposited on single-crystal, *n*-type Si (100) substrates with relatively high resistivities of 4 to 30 Ω×cm.[23-25, 49]

Thus, formation of the metastable, orthorhombic phase was proposed to result from direct epitaxy between the Si (100) substrate and the growing film. A unified mechanism for controlling the phase selectivity in this material system has not yet been developed. Furthermore, while orthorhombic Bi_2Se_3 is of potential interest for optoelectronic and thermoelectric devices, the requirement to deposit on single-crystal Si substrates limits the ability to measure fundamental properties of this metastable material and determine its suitability for these applications.

In this Article, we demonstrate that the spontaneous formation of a seed layer during the electrodeposition of bismuth selenide, Bi_2Se_3, enforces growth of the metastable orthorhombic phase through epitaxial strain. Seeded epitaxial growth enables us to electrodeposit this semiconductor with high crystallinity, which is not typically observed in electrodeposition. We first determined the phase of Bi_2Se_3 films that were electrodeposited on single-crystal silicon substrates with a range of resistivities and different orientations. By varying the applied potential used to grow the films, we identified that formation of a previously unrecognized seed layer — with a distinct composition and structure from that of Bi_2Se_3 — is necessary to produce the metastable orthorhombic phase. Through transmission electron microscopy, we uncovered that the seed layer contains nanocrystals of cubic BiSe. Orthorhombic Bi_2Se_3 microcrystals nucleate from the BiSe nanocrystals and grow along the [010] direction. Our experimental results are supported by first-principles calculations that show the epitaxial strain between cubic BiSe and orthorhombic Bi_2Se_3 is much smaller than that between cubic BiSe and the thermodynamically stable, rhombohedral phase of Bi_2Se_3. This model of seeded epitaxial growth not only explains the formation of the metastable phase but also accounts for the experimental growth direction of the orthorhombic Bi_2Se_3 crystals. The spontaneous formation of a seed layer alleviates the need to use a single-crystal substrate for electrodeposition, enabling the growth of metastable, orthorhombic

Bi_2Se_3 microcrystals for the first time on polycrystalline substrates including gold and fluorine-doped tin oxide. Our results demonstrate the feasibility of electrodepositing metastable structures with high crystallinity on polycrystalline substrates by using nanocrystal seeds (rather than a single-crystal substrate) to induce epitaxy and enforce the desired phase.

Results and Discussion

We first electrodeposited Bi_2Se_3 films on single-crystal silicon substrates with different orientations and resistivities and characterized the crystalline phase of the resulting films. The films were grown at a constant applied potential, and the total charge passed between the working and counter electrodes was varied to control the amount of material deposited (see **Figure S1** for representative current traces during film deposition). X-ray diffraction (XRD) patterns of Bi_2Se_3 films grown at a potential of -0.45 V vs. an Ag/AgCl reference electrode for a total charge density of 2 C/cm^2 are shown in **Figure 1b**. Using either Si (100) substrates with a resistivity of 4.4 Ω×cm or Si (111) substrates with a resistivity of 1.3 Ω×cm, we consistently observed that the Bi_2Se_3 films grew in the orthorhombic phase at this potential. On the other hand, using Si (111) substrates with a higher dopant density and a resistivity of 0.0061 Ω×cm, the Bi_2Se_3 films consistently grew in the rhombohedral phase at -0.45 V vs. Ag/AgCl. These results show that the phase of the Bi_2Se_3 films can be controlled by the resistivity of the substrate.

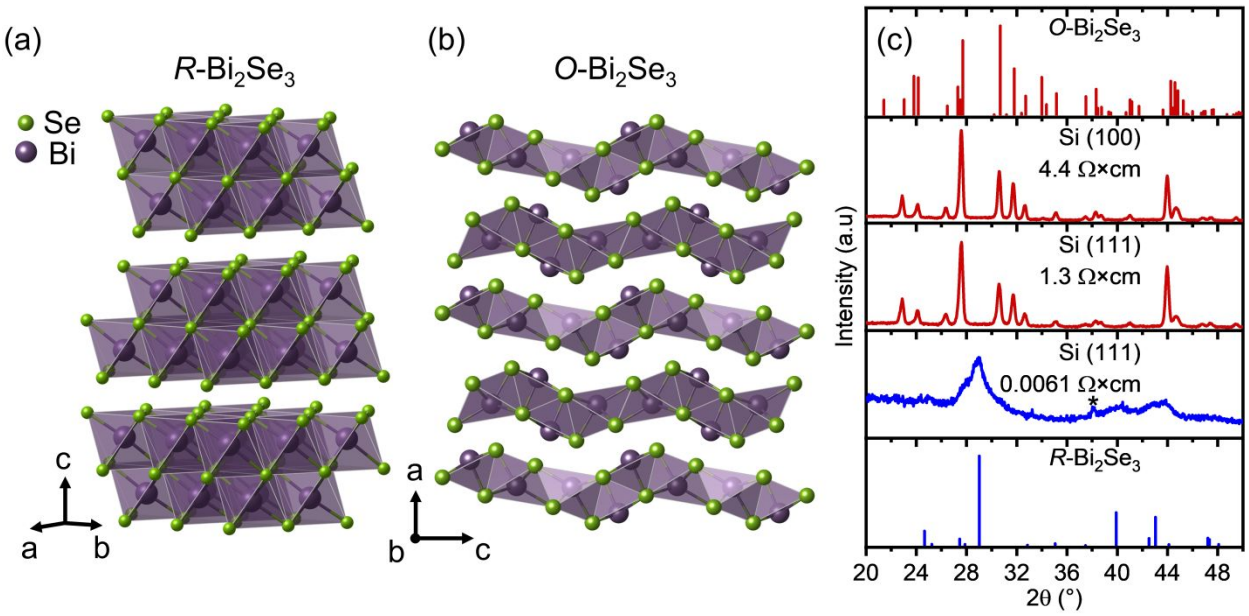

Figure 1. Atomic structures of (a) the stable, rhombohedral phase of Bi_2Se_3 (collection code #165226, *R*-Bi_2Se_3) and (b) metastable, orthorhombic phase of Bi_2Se_3 (collection code #617093, *O*-Bi_2Se_3). The initial structures come from the Inorganic Crystal Structure Database (ICSD)[56] and were relaxed using density-functional theory. (c) Thin-film XRD patterns of Bi_2Se_3 films grown on single-crystal Si substrates with different orientations and resistivities. The applied potential used to grow each film was -0.45 V vs. Ag/AgCl, and the total amount of charge passed was 2 C/cm^2. The asterisk marks an impurity, the (111) peak of Ag, which was used to make electrical contact to the Si substrate (see the **Experimental section** for more details on electrode and sample preparation). The top, red pattern is the standard XRD powder pattern of orthorhombic Bi_2Se_3 (PDF #04-003-6014), and the bottom, blue pattern is the standard XRD powder pattern of rhombohedral Bi_2Se_3 (PDF #04-002-5483). Experimental patterns in red denote growth of *O*-Bi_2Se_3, and the pattern in blue denotes *R*-Bi_2Se_3.

Table 1. Summary of the crystalline phases of Bi_2Se_3 films grown via electrodeposition at a constant potential on single-crystal Si substrates with different orientations and resistivities. *O* indicates the orthorhombic phase. *R* indicates the rhombohedral phase. *R*/*O* indicates the film is a mixture of the rhombohedral and orthorhombic phases. None indicates there was no observable film formation (or that the deposited material fell off the substrate during deposition). Deposition at a potential of -0.48 V vs. Ag/AgCl was only performed on the Si substrates with resistivities of 1.3 and 0.56 Ω×cm. The standard deviation in the resistivity of each Si substrate was determined by measuring four different areas of the same substrate.

Substrate orientation	Substrate resistivity (Ω×cm)	Phase formed at various potentials (vs. Ag/AgCl)							Reduction peak (V vs. Ag/AgCl) in $Bi(NO_3)_3$ solution
		-0.50 V	-0.48 V	-0.45 V	-0.30 V	-0.20 V	-0.10 V	0.00 V	
(100)	4.4±0.2	None	-	*O*	*O*	None	None	None	-0.53
(111)	3.6±0.1	None	-	*O*	*O*	None	None	None	-0.50
(111)	1.3±0.1	*R*	*R*/*O*	*O*	*O*	None	None	None	-0.41
(100)	0.56±0.01	*R*	*R*	*R*/*O*	*O*	None	None	None	-0.40
(111)	0.0041±0.0003	None	-	*R*	*R*	*R*	*O*	*O*	-0.11
(100)	0.0032±0.0001	None	-	*R*	*R*	*R*	*O*	*O*	-0.11

We next varied the applied potential used to grow the Bi_2Se_3 films. **Table 1** provides a summary of the phases formed on single-crystal Si substrates with different orientations and resistivities. XRD patterns for each sample listed in **Table 1** are provided in **Figures S2 – S7** of the **Supporting Information**. For Si substrates with the highest resistivities (3.6 and 4.4 Ω×cm), we could only electrodeposit Bi_2Se_3 films within a narrow potential range. Deposition at potentials more negative than -0.45 V vs. Ag/AgCl led to delamination of the film during growth, while no growth was observed at potentials positive of -0.30 V vs. Ag/AgCl. At potentials of -0.30 and -0.45

V vs. Ag/AgCl, we observed the metastable, orthorhombic phase (**Figures S6** and **S7**). For Si substrates with lower resistivities, we found that we could control the resulting phase based on the applied potential. For Si (111) substrates with a resistivity of 1.3 Ω×cm, films grown at -0.30 and -0.45 V vs. Ag/AgCl exhibited the orthorhombic phase of Bi_2Se_3. At -0.48 V vs. Ag/AgCl, the films consisted of a mixture of orthorhombic and rhombohedral phases. At -0.50 V, the films exhibited the rhombohedral phase (**Figure S5**). For orthorhombic Bi_2Se_3 films, we did not observe the formation of any compounds other than Bi_2Se_3 by XRD. For rhombohedral Bi_2Se_3 films grown at more negative potentials (-0.45 to -0.50 V), we observed the presence of elemental selenium as a minor impurity phase (**Figures S3** and **S4**). As the resistivity of the Si substrate decreased, the transition between the two phases shifted to more positive potentials. For Si (100) substrates with a resistivity of 0.56 Ω×cm, the transition from orthorhombic to rhombohedral phases was between -0.30 and -0.48 V vs. Ag/AgCl (**Figure S4**). For Si (100) substrates with a resistivity of 0.0032 Ω×cm and Si (111) substrates with a resistivity of 0.0041 Ω×cm, the orthorhombic phase was observed at potentials of 0.00 and -0.10 V vs. Ag/AgCl. However, films grown at potentials of -0.20, -0.30, and -0.45 V vs. Ag/AgCl exhibited the rhombohedral phase (**Figures S2** and **S3**). Our results demonstrate that the combination of applied potential and the resistivity of the Si substrate, rather than its orientation, control the resulting phase of the Bi_2Se_3 films. Si substrates with similar resistivities but different orientations produce the same phase at a given potential.

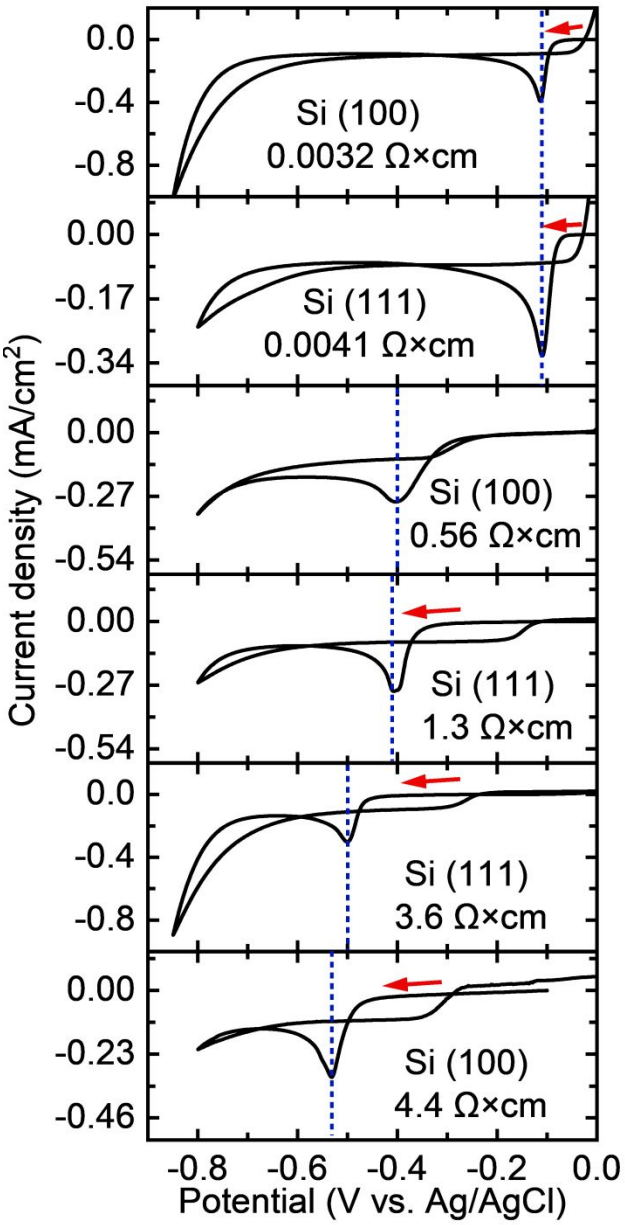

Figure 2. Cyclic voltammograms in an aqueous solution of 1 mM $Bi(NO_3)_3$ and 0.5 M HNO_3 using single-crystal Si electrodes with different orientations and resistivities. Each Si electrode was first swept from the open-circuit potential to 0 V vs. Ag/AgCl (not shown) followed by scanning towards more negative potentials (red arrows). The scan rate was 20 mV/s. The blue dashed lines indicate the positions of the redox wave corresponding to the reduction of Bi^{3+} to Bi^0 during the initial negative sweep, which are listed in **Table 1**.

The resistivity of the Si substrate determines the potential at which Bi is deposited on the electrode and correlates with the resulting phase of the Bi_2Se_3 film. We used cyclic voltammetry (CV) to determine the reduction potential of Bi^{3+} using Si substrates with different resistivities as the working electrode. The solution used for CV contained $Bi(NO_3)_3$ at the same concentration and pH used to deposit the Bi_2Se_3 films (but without SeO_2). The overpotential for the reduction of Bi^{3+} increases as the resistivity of the working electrode increases, as shown in **Figure 2**. The peak maxima for the redox wave corresponding to the reduction of Bi^{3+} shift to more negative values for Si substrates with higher resistivities.

We find that the Bi_2Se_3 films grow in the orthorhombic phase when the applied potential during film growth is close to or positive of the peak potential for Bi^{3+} reduction. For example, using an Si (111) substrate with a resistivity of 1.3 Ω×cm, the Bi^{3+} reduction peak occurs at -0.41 V vs. Ag/AgCl (see **Figure 2**). The orthorhombic phase is formed at a potential of -0.45 V vs. Ag/AgCl, while the rhombohedral phase is formed at -0.50 V vs. Ag/AgCl (**Figure S5**). For both an Si (100) substrate with a resistivity of 0.0032 Ω×cm and an Si (111) substrate with a resistivity of 0.0041 Ω×cm, the Bi^{3+} reduction peak occurs at -0.11 V vs. Ag/AgCl. The orthorhombic phase is formed at potentials of 0.00 and -0.10 V vs. Ag/AgCl for both substrates, while the rhombohedral phase occurs at more negative potentials of -0.20, -0.30, and -0.45 V vs. Ag/AgCl (**Figures S2** and **S3**). Thus, when the applied potential is sufficiently more negative than the Bi^{3+} reduction peak, the rhombohedral phase is formed. In solutions containing only SeO_2, we found that the reduction peak for Se^{4+} was approximately -0.6 V vs. Ag/AgCl for all Si substrates as shown in **Figure S8**. As described further below, growing Bi_2Se_3 films at a potential close to or positive of the reduction

peak for Bi^{3+} leads to a Bi-rich film during the early stages of growth, which is observed for all films having the orthorhombic phase.

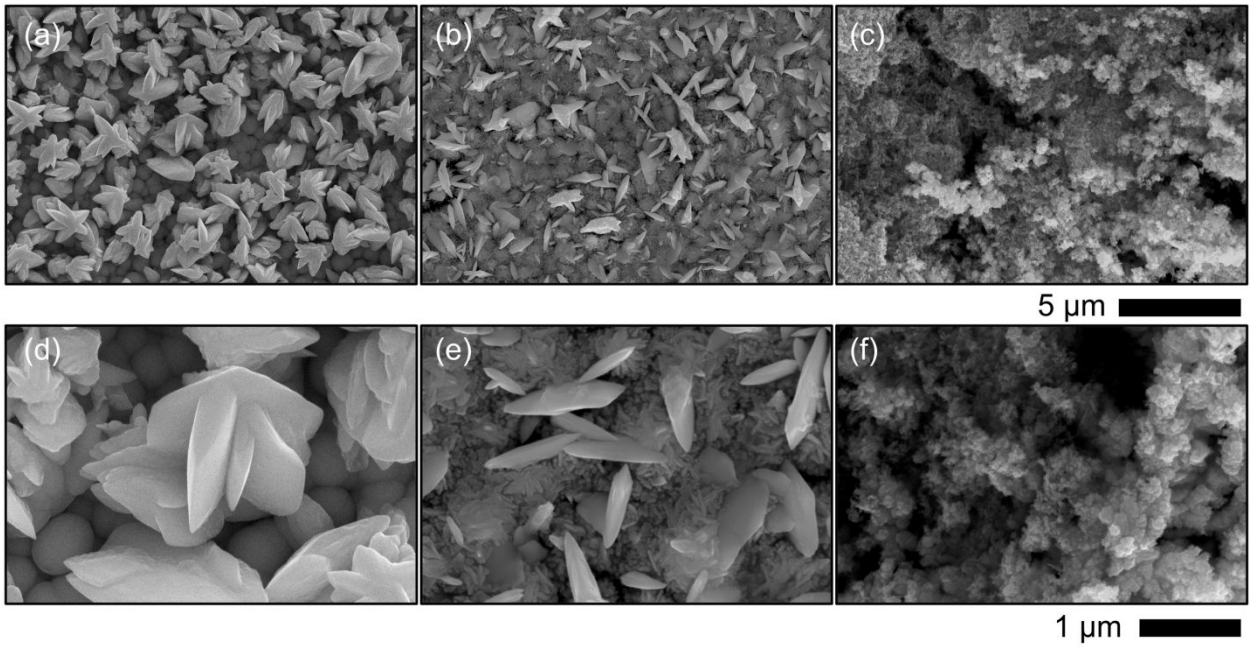

Figure 3. SEM images of Bi_2Se_3 films grown on single-crystal Si substrates with different orientations and resistivities. (a, d) Low- and high-magnification SEM images of a Bi_2Se_3 film grown on a Si (111) electrode with a resistivity of 1.3 Ω×cm at a potential of -0.30 V vs. Ag/AgCl for a total charge density of 2 C/cm^2. These conditions produce films with the orthorhombic phase as measured by XRD (see **Figure S5**). (b, e) SEM images of a Bi_2Se_3 film grown on a Si (100) electrode with a resistivity of 0.0032 Ω×cm at a potential of -0.10 V vs. Ag/AgCl for a total charge density of 2 C/cm^2. These conditions produce films with the orthorhombic phase (see **Figure S2**). (c, f) SEM images of a Bi_2Se_3 film grown on a Si (100) electrode with a resistivity of 0.0032 Ω×cm at a potential of -0.30 V vs. Ag/AgCl for a total charge density of 2 C/cm^2. These conditions produce films with the rhombohedral phase (see **Figure S2**). The scale bars of 5 μm and 1 μm apply to the top row and bottom row of images, respectively.

Bi_2Se_3 films with the orthorhombic phase possess larger crystallite sizes than those with the rhombohedral phase. **Figure 3** shows representative scanning electron microscopy (SEM) images of films grown on different single-crystal Si substrates. Films with the orthorhombic phase consist of interleaved platelets with microscale dimensions, as shown in **Figure 3a, d**. These platelets grow out of a dense layer of hemispherical seed particles that can be seen underneath the platelets in **Figure 3a, d** (see also **Figure S9**). The platelet morphology is observed for orthorhombic Bi_2Se_3 films grown on both Si (111) (**Figure 3a, d**) and Si (100) substrates (**Figure 3b, e**), which reinforces that epitaxy with the Si (100) surface is not necessary to produce the orthorhombic phase. In sharp contrast, films with the rhombohedral phase consist of aggregated nanoscale crystallites (**Figure 3c, f** and **Figure S10**). Consistent with the SEM images, XRD patterns show broader peaks for films with the rhombohedral phase compared to the orthorhombic phase (see **Figure 1b** and **Figures S2 – S5**). Furthermore, the relative intensities of peaks in the thin-film XRD patterns for the orthorhombic phase show texture effects indicating that the crystals have a preferred orientation. Notably, the (020) peak at 44° shows a higher relative intensity compared to the standard powder pattern (**Figure 1c**). While the (112) peak at 27.6° also shows a higher relative intensity, we found that the intensity of this peak varies for different entries of orthorhombic Bi_2Se_3 in the ICSD.

The morphological evolution of Bi_2Se_3 films with the orthorhombic phase, as characterized using SEM imaging, is shown in **Figure 4**. These samples were grown on Si (111) substrates with a resistivity of 3.6 Ω×cm at a potential of -0.45 V vs. Ag/AgCl for different amounts of charge passed. For a charge density of 0.3 C/cm^2, the film consists of a layer of sub-micron-sized hemispherical seeds that cover the Si substrate (with some exposed regions of the substrate as

shown in the top-down SEM image in **Figure 4a**). At this stage of growth, the seeds have an elemental Se:Bi ratio of 1.3 as determined by energy dispersive x-ray (EDX) spectroscopy. The seeds are rich in bismuth relative to the Se:Bi ratio of 1.5 in Bi_2Se_3. Thin-film XRD patterns do not show any distinct diffraction peaks at this stage of growth, indicating the initial seed layer has low crystallinity (see **Figure S9**). For a charge density of 0.5 C/cm^2, the Se:Bi ratio is still 1.3, but platelet crystallites have nucleated from the hemispherical seeds (**Figure 4b**). The platelets continue to grow with the amount of charge passed; the platelets also branch, and new platelets nucleate from the seed layer. The films have the expected Se:Bi ratio of 1.5 for a charge density of 0.9 C/cm^2 (**Figure 4c**). However, the films eventually become rich in Se with an elemental Se:Bi ratio of 1.8 at a charge density of 1.1 C/cm^2 (**Figure 4d**). The excess Se relative to the ratio for Bi_2Se_3 indicates the co-deposition of elemental selenium, which is supported by x-ray photoelectron spectroscopy (XPS) (see **Figure S12**). Films grown on other Si substrates at potentials that produce the orthorhombic phase exhibit a similar evolution in their morphology.

Films possessing the rhombohedral phase undergo a very different growth pattern. Unlike the growth of the orthorhombic phase, there is no seed layer at the early stages of growth. Aggregated nanoscale crystallites form directly on the Si electrode. The aggregates become denser until they cover the Si substrate and continue to grow out from the surface of the electrode with increasing deposition times (see **Figure S10**). Unlike the orthorhombic films, films with the rhombohedral phase are rich in selenium relative to the stoichiometry of Bi_2Se_3 at all stages of growth (**Figures S10** and **14b**).

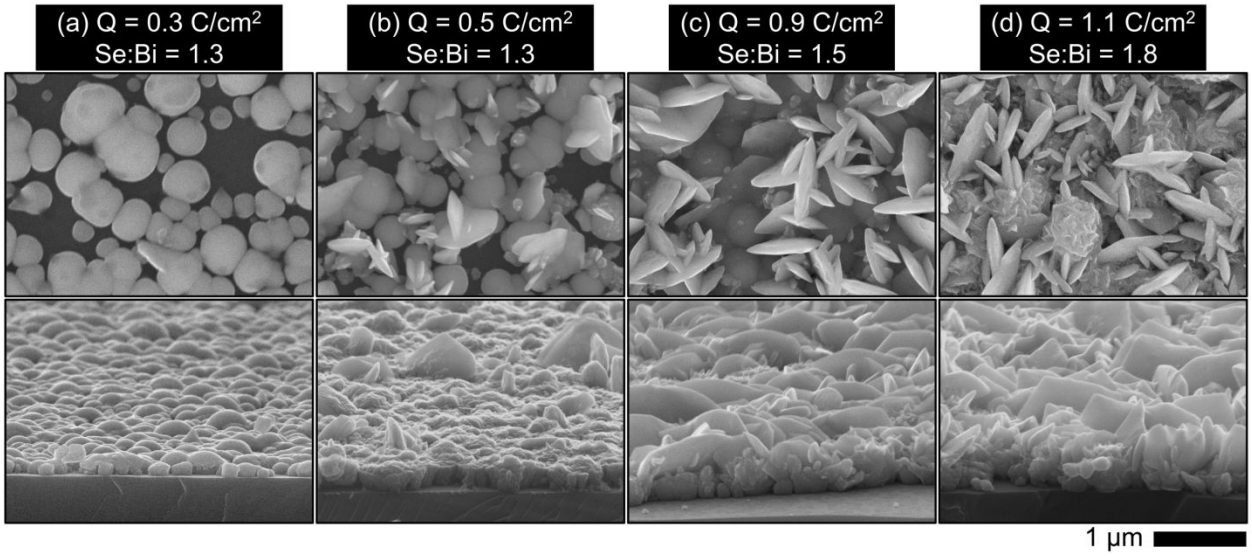

Figure 4. SEM images of Bi_2Se_3 films grown on Si (111) electrodes with a resistivity of 3.6 Ω×cm at a potential of -0.45 V vs. Ag/AgCl for total charge densities of (a) 0.3 C/cm^2; (b) 0.5 C/cm^2; (c) 0.9 C/cm^2; (d) 1.1 C/cm^2. These growth conditions produce films with the orthorhombic phase as determined by XRD (see **Figure S6**). For each sample, a top-down image is shown in the top row, and a cross-sectional image is shown in the bottom row. The scale of 1 μm applies to all images.

The essential difference between formation of the orthorhombic and rhombohedral phases appears to be the amorphous seed layer that forms during the initial stage of growth for the orthorhombic phase. To characterize the seed layer, we next conducted XPS of Bi_2Se_3 films grown on Si (100) electrodes with a resistivity of 4.4 Ω×cm, which is a representative case that results in the growth of the orthorhombic phase as determined by XRD (see **Figure S7**). The films were first sputtered to remove the surface oxide layer that forms over time when the samples are left out in air (**Figure S11**). By fitting the peaks in the binding region of Bi $4f_{5/2}$ and $4f_{7/2}$ electrons, we observe varying contributions from Bi^{3+} as well as Bi in both lower and higher oxidation states in films grown for different amounts of time (**Figure 5**). The most prominent contribution for all

films is Bi^{3+}, consistent with the formation of Bi_2Se_3.[57] The weak peaks at higher binding energies, labeled $Bi^{(3+x)+}$, that are observed at all deposition times could arise from either Bi^{5+} or Bi^{3+} bonded to residual oxygen (see **Supporting Discussion S1** in the **SI** for further details).[55, 57-58] There are also minor peaks from Bi in a lower oxidation state, labeled as $Bi^{(3-x)+}$,[59-61] which are most prominent for the earliest stage of growth (0.3 C/cm^2) measured, but disappear by the final stage (2 C/cm^2). Bader charge analysis of a series of bismuth selenide and oxide compounds is consistent with these assignments (see **Supporting Discussion S1**, **Table S4**, and **Figure S15**). We observe the contribution from $Bi^{(3-x)+}$ in films that exhibit the orthorhombic phase on other Si substrates, as well as the decrease in its contribution with growth time (**Figure S13a**). On the other hand, while films with the rhombohedral phase show a minor contribution from $Bi^{(3-x)+}$ at later stages of growth, this oxidation state does not appear during the early stages of growth (**Figure S14a**).

Comparing XPS in **Figure 5** to the SEM images in **Figure 4**, when the amorphous, Bi-rich seed layer is formed during the early stages of deposition (i.e., 0.3 and 0.5 C/cm^2 of charge passed), the films contain Bi in a lower oxidation state (in addition to the Bi^{3+} and $Bi^{(3+x)+}$ states). As the orthorhombic crystallites nucleate and grow from the seed layer, the overall composition becomes closer to Bi_2Se_3 matching the orthorhombic phase observed by XRD. XPS in the region of Se 3*d* states shows that the co-deposition of Se metal leads to Se-rich films relative to Bi_2Se_3 (i.e., Se:Bi > 1.5) during the final stages of growth (see **Figure S12**). The combined characterization by XRD, EDX spectroscopy, SEM, and XPS, point towards the formation of an intermediate bismuth selenide compound during the early stages of growth with a distinct structure and composition from that of Bi_2Se_3 that induces formation of the metastable orthorhombic phase of Bi_2Se_3.

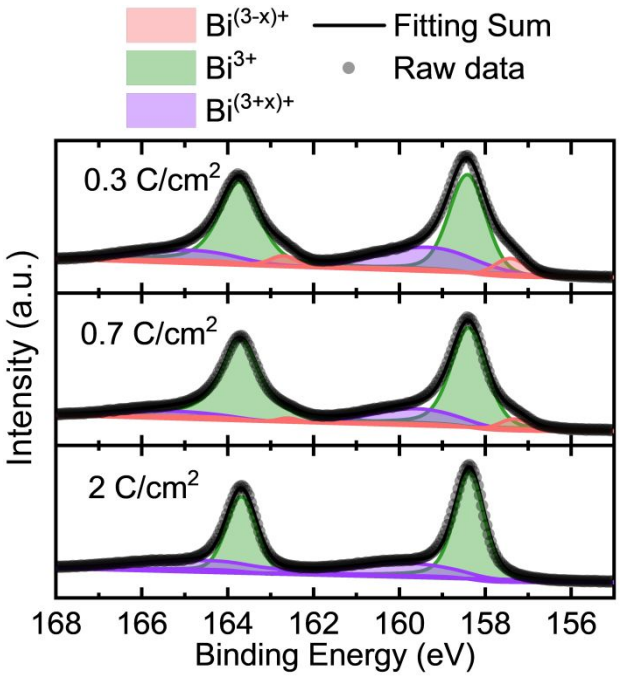

Figure 5. XPS of Bi_2Se_3 films showing the binding energy region for Bi 4*f* electrons. The films were grown on Si (100) substrates with a resistivity of 4.4 Ω×cm at a potential of -0.45 V vs. Ag/AgCl for different charge densities. These growth conditions produce films with the orthorhombic phase (see **Figure S7**). The shaded regions show the deconvolution of the peaks into contributions from $Bi^{(3+x)+}$ (purple), Bi^{3+} (green), and $Bi^{(3-x)+}$ (light red). The gray points show the raw data, and the black lines show the sum of fitting the peaks to the different oxidation states of Bi.

We used transmission electron microscopy (TEM) to gain further insights into the structure of the seed layer that produces orthorhombic Bi_2Se_3 crystals. A cross-sectional, bright-field image of the interfacial region between the seed layer and two orthorhombic crystallites that share a twin boundary is shown in **Figure 6a**. An electron diffraction pattern of the seed layer (indicated by the white circle in **Figure 6a**) is shown in **Figure 6b**. The pattern shows two relatively sharp rings,

which indicates the likely presence of randomly oriented nanocrystals within the amorphous seed layer.[62] We find the radius of the inner ring to be 3.4 ± 0.1 nm^{-1} and that of the outer ring to be 4.8 ± 0.2 nm^{-1}, which provide the nearest and second-nearest neighbor distances between atoms in the nanocrystals. Furthermore, we observed several nanocrystals embedded within the amorphous seed layer in a dark-field TEM image shown in **Figure S18b**— that was obtained using a diffracted beam from an adjacent Bi_2Se_3 crystallite. To further characterize the structure of the nanocrystals within the seed region, we performed electron diffraction on a film where the deposition was terminated at the formation of the seed layer (i.e., before nucleation of the orthorhombic crystallites). For this sample, the seed layer was scraped off from the Si substrate and transferred to a TEM grid. The electron diffraction pattern of the sample at this stage of growth is shown in **Figure 6c**. The pattern shows four main spots in the inner ring with 4-fold symmetry and a reciprocal spacing of 3.49 nm^{-1} that matches the spacing of the inner ring in the cross-sectional sample. To identify the structure of these nanocrystals, we searched for all experimentally reported compounds of Bi and Se in the ICSD (see **Table S5**) and simulated their diffraction patterns to compare them to our experimental pattern. We find that BiSe with the rock salt structure ($Fm\bar{3}m$) provides the best match. An atomic model of cubic BiSe is shown in **Figure S16**. A simulated electron diffraction pattern along the [100] zone axis for the structure obtained from the ICSD is shown in **Figure 6d**. We find the reciprocal lattice spacings of the (002) and (202) planes are 3.34 nm^{-1} and 4.72 nm^{-1}, respectively, which match well with the spacings of the 1st and 2nd rings in the experimental pattern in **Figure 6b**. Among the compounds searched, the only other structure that possesses a four-fold symmetry is Bi_2Se_3 with the Zn_3P_2 structure ($P4_2/nmc$). However, its simulated diffraction pattern does not match the experimental lattice spacings, as shown in **Figure S17**. Based on the good agreement between the simulated and experimental diffraction patterns

and the nanocrystals with bright contrast in the dark-field image (**Figure S18b**), we propose the intermediate Bi–Se compound, critical for the formation of the orthorhombic phase, consists of nanocrystals of cubic BiSe nanocrystals embedded within a Bi-rich, amorphous seed layer that initially deposits on the Si electrode. This hypothesis is consistent with the lower Se:Bi ratio observed for the seed region using EDX spectroscopy (**Figure 4a**). Furthermore, Bader charge analysis of BiSe indicates that it is responsible for the $Bi^{(3-x)+}$ peaks observed in XPS during the early stages of growth (see **Supporting Discussion S1**, **Table S4**, and **Figure S15**).

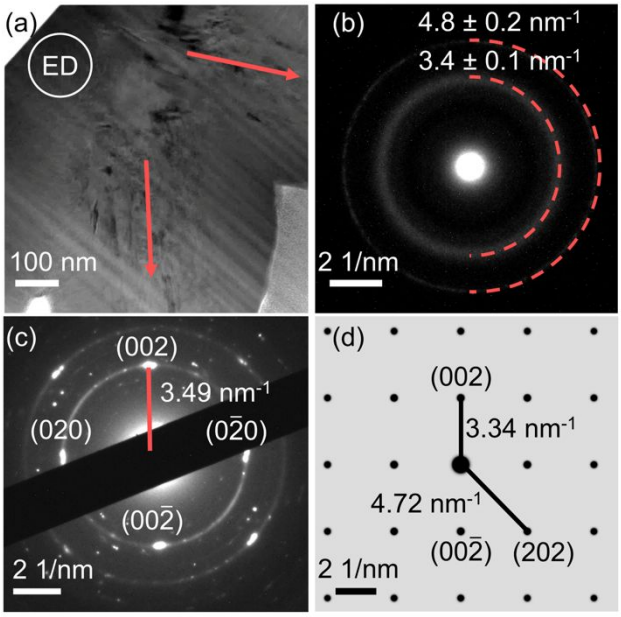

Figure 6. (a) Cross-sectional, bright-field TEM image of an orthorhombic Bi_2Se_3 film grown on a Si (111) electrode with a resistivity of 1.3 Ω×cm at a potential of -0.30 V vs. Ag/AgCl for a charge density of 0.9 C/cm^2. The red arrows indicate the growth directions of the two crystallites separated by a twin boundary. (b) Electron diffraction pattern of a region on the same film near the interface with the Si growth substrate. The white circle in panel (a) indicates the area used to obtain the electron diffraction pattern of the cross section shown in (b). (c) Electron diffraction pattern of a

separate sample grown on a Si (111) electrode with a resistivity of 0.0061 Ω×cm at a potential of -0.10 V vs. Ag/AgCl for a charge density of 0.2 C/cm^2. To obtain the electron diffraction pattern, the film was scraped off the Si substrate and transferred to a TEM grid. (d) Simulated electron diffraction pattern of cubic BiSe along the [100] zone axis.

Having established the structure of the seed region, we next characterized the growth directions of the twinned orthorhombic Bi_2Se_3 crystals that nucleate from the seed region, as shown in **Figure 7**. Dark-field TEM images of the two adjacent orthorhombic Bi_2Se_3 crystallites are shown in **Figure 7a** and **d**. Electron diffraction patterns of each crystallite were obtained by tilting the respective grains so that they are oriented along the [110] and [001] zone axes, respectively, as shown in **Figure 7b** and **e**. High-resolution TEM images of the two grains that are oriented along the [110] and [001] zone axes are shown in **Figure 7c** and **f**, respectively. From the lattice spacings, we derived the lattice planes in the corresponding images to be (001) and (200), respectively. We find the growth direction of the two crystallites to be along the [010] axis (red arrows in **Figure 7c** and **f**) from the intersection between the (001) and (200) planes, as shown schematically in **Figure 7g**.

The formation of such oriented crystallites can occur through two scenarios: (I) if the (010) surface of orthorhombic Bi_2Se_3 has a significantly lower energy than the other surfaces; or (II) if there is epitaxy between the orthorhombic Bi_2Se_3 crystallites and the BiSe nanocrystals embedded in the seed layer. We used density-functional theory (DFT) to calculate the surface energies of various low-index surfaces of Bi_2Se_3 in the orthorhombic and rhombohedral phases as well as cubic BiSe. We find that the (010) surface of orthorhombic Bi_2Se_3 has the highest surface energy compared to the (100) and (001) surfaces, as shown in **Table S6**. We can therefore rule out scenario

I. In support of scenario II, we obtained an electron diffraction pattern from a region at the intersection of the two orthorhombic Bi_2Se_3 crystallites, shown in **Figure S18**. We find that the two grains share a twin boundary at the $(1\bar{1}5)$ plane. The lattice parameters along the [100] and [001] directions of orthorhombic Bi_2Se_3 are similar (11.66 Å and 11.45 Å). So, in some cases, the Bi_2Se_3 lattice can deform along [100] to match with the cubic symmetry of underlying BiSe, while in other cases, it can deform along [001]. When these different crystallites grow to merge, they can result in the formation of a twin boundary, as we observe experimentally. Thus, the presence of oriented and twinned crystallites of orthorhombic Bi_2Se_3 suggest that the nucleation and growth of Bi_2Se_3 occurs epitaxially from the cubic BiSe nanocrystals in the seed layer.

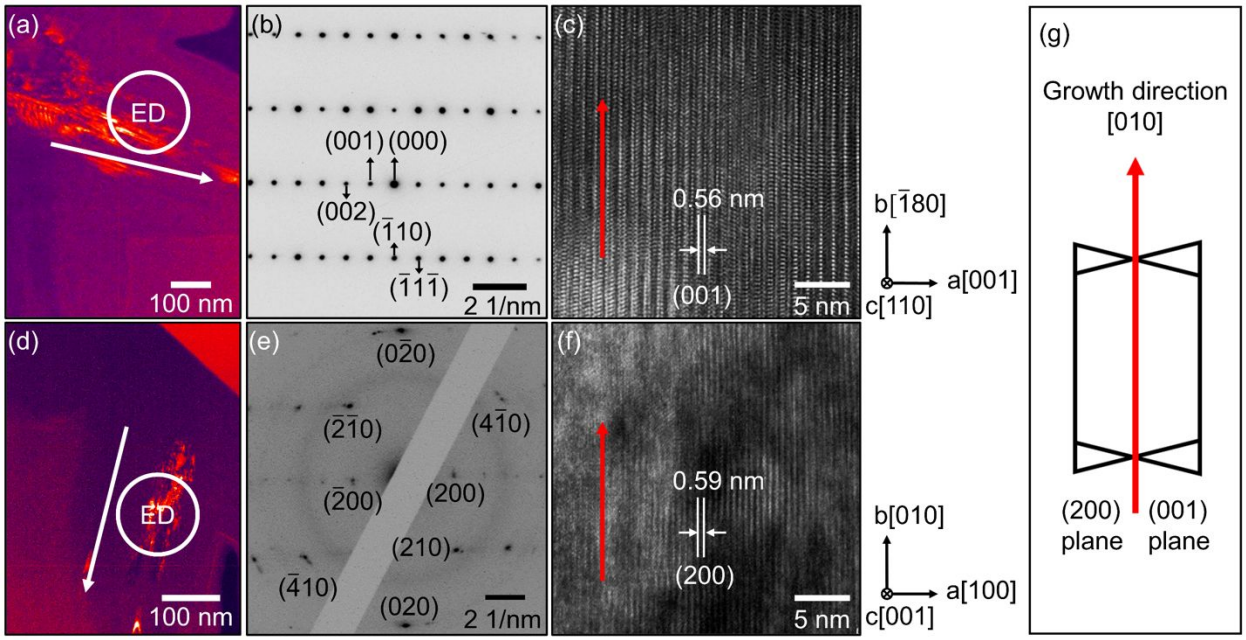

Figure 7. Cross-sectional TEM images and electron diffraction patterns of the twinned orthorhombic Bi_2Se_3 crystallites that grew from the seed region shown in **Figure 6a**. (a, d) Dark-field cross-sectional TEM images of the two orthorhombic Bi_2Se_3 crystallites. The white circles in panels (a) and (d) indicate the selected areas used to obtain electron diffraction patterns shown in

panels (b) and (e) and high-resolution TEM images in panels (c) and (f), respectively. The white arrows indicate the growth direction of each crystallite. (b, e) Electron diffraction patterns for the two orthorhombic Bi_2Se_3 crystallites. (c, f) High-resolution bright-field TEM images of the two orthorhombic Bi_2Se_3 crystallites showing (001) and (200) lattice planes that are parallel to the growth directions of the crystallites, which point upward (red arrows). (g) A schematic showing the growth of the two twinned crystallites along with their growth direction.

We next used DFT calculations to identify the preferred epitaxial relationship between cubic BiSe and both orthorhombic and rhombohedral Bi_2Se_3 along with the energy of the two phases under varying epitaxial strains. From the calculated surface energy of the common facets of cubic BiSe, and orthorhombic and rhombohedral Bi_2Se_3, which are shown in **Table S6**, we find that the (001) surface of BiSe has the lowest energy followed by the (110) and (111) surfaces, respectively. Hence, we modeled the growth of Bi_2Se_3 on the (001) and (110) surfaces of BiSe. We discuss the results on the (001) surface below and present the results on the (110) surface in the **Supporting Information Figure S20**. For rhombohedral Bi_2Se_3, which has a layered structure, the (001) surface has a surface energy that is significantly smaller than the other facets due to the weak interlayer bonding along [001]. Hence, we expect it to serve as the growth plane for rhombohedral Bi_2Se_3. We next built coincident site lattice models between the (001) plane of BiSe and the (001) plane of rhombohedral Bi_2Se_3, as shown in **Figure S19**. According to coincident site lattice theory, epitaxial interfaces are formed by constraining the film to match the substrate along special orientations where the lattice sites of the film and the substrate coincide.[21, 26, 63] We tried two different orientations for the rhombohedral Bi_2Se_3 (001) surface on top of the BiSe (001) surface, as shown in **Figure S19**. We further varied the lattice parameter of BiSe (001) to account for the

uncertainty in the lattice parameter of the BiSe nanocrystals — that may arise from their extremely small size and variable composition, which are challenging to be characterized accurately — and accordingly varied the epitaxial strain on Bi_2Se_3 (see the **Calculation methods** in the **Experimental section** for more details). The stabilities of orthorhombic and rhombohedral Bi_2Se_3 with different orientations and epitaxially matched to BiSe (001) are shown in **Figure 8**. We find that the model having the [100] direction of rhombohedral Bi_2Se_3 orientated along the [001] direction of BiSe minimizes the epitaxial strain. However, even for this configuration, rhombohedral Bi_2Se_3 experiences a tensile strain of 19% to match the BiSe (001) surface, when using the theoretical lattice parameters for both the phases. These results suggest that rhombohedral Bi_2Se_3 is unlikely to be epitaxially stabilized on BiSe.

We next built coincident site lattice models between the (010), (100), (001), and (201) surfaces of orthorhombic Bi_2Se_3 — that have surface energies ranging between 20.1 – 48 meV/Å^2, as listed in **Table S6**— and (001) BiSe, as shown in **Figure S19**. We applied biaxial strain to orthorhombic Bi_2Se_3 along the two axes of the surfaces shown in the atomic models in **Figure 8.** For the (010) surface of orthorhombic Bi_2Se_3 to match with the BiSe (001) surface, the lengths along the [100] and [001] axes of Bi_2Se_3 were adjusted to be 2 times the lattice parameter of the BiSe substrate, as shown in **Figure S19** and described in the **Calculation methods**. We then uniformly varied the lattice parameter of BiSe around its minima to simulate a range of epitaxial strains on the Bi_2Se_3 film. This changes the strain along the [100] and [001] axes of the orthorhombic Bi_2Se_3 (010) surface according to the relationship discussed above. The formation enthalpy of (010) Bi_2Se_3 as a function of strain for epitaxy on BiSe (001) is shown in **Figure 8**. We have followed a similar procedure to calculate the formation enthalpies of orthorhombic Bi_2Se_3 with (100), (001), and (201) surfaces as the growth plane that are epitaxially matched with BiSe (001) for varying epitaxial

strains, and the results are also shown in **Figure 8**. We find that the orthorhombic Bi_2Se_3 phase with (010) growth surface has the lowest formation enthalpy as the substrate lattice parameter varies from 5.40 Å to 5.94 Å. When the BiSe lattice parameter varies from 5.94 Å to 6.19 Å, the orthorhombic Bi_2Se_3 phase with (001) surface has the lowest formation energy. The experimental reciprocal spacing of cubic BiSe (002) planes is 3.49 nm^{-1}, which corresponds to a unit cell length of 5.73 Å for BiSe. For a BiSe substrate lattice parameter, a_{sub} = 5.73 Å, orthorhombic Bi_2Se_3 with the (010) growth surface has the lowest formation enthalpy, which agrees with the experimentally observed phase and growth direction using TEM. Overall, our calculations show that for a large range of lattice parameters of BiSe, the orthorhombic phase of Bi_2Se_3 can be stabilized over the rhombohedral phase through epitaxy, and the preferred growth direction of the orthorhombic phase is [010] when it grows on the BiSe (001) surface.

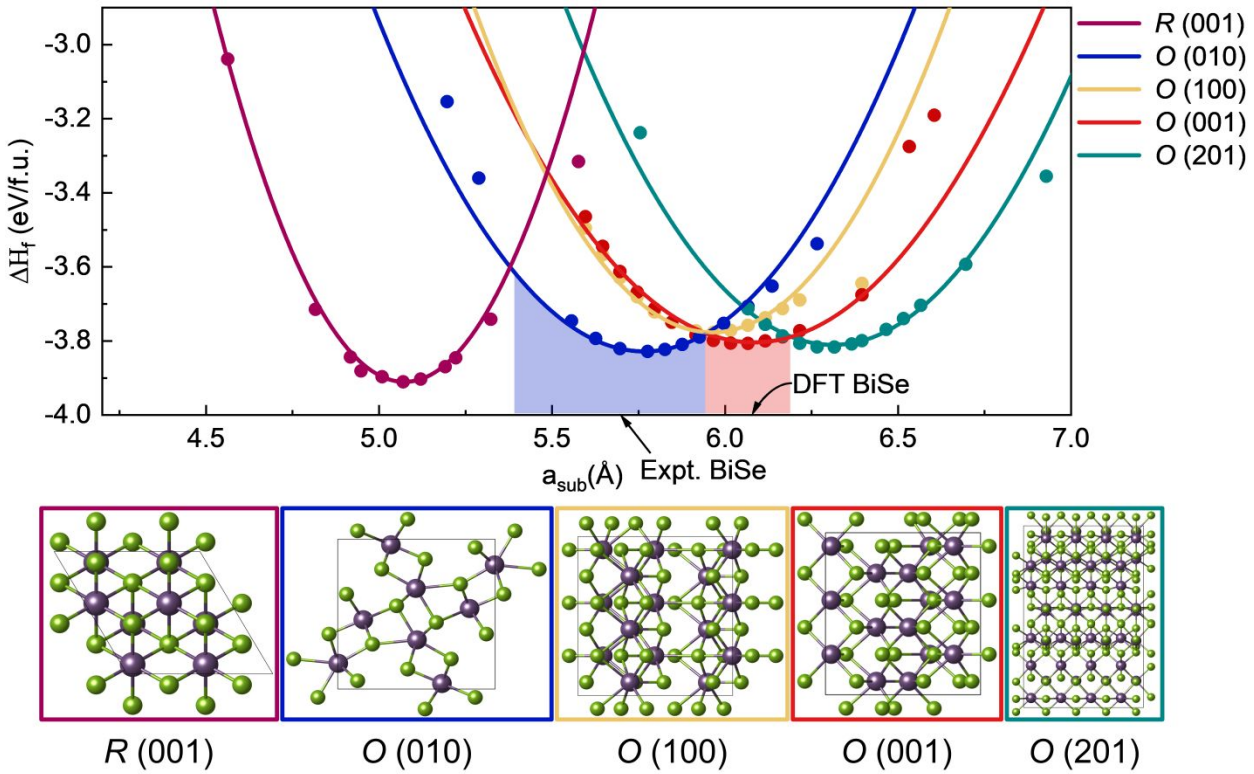

Figure 8. (Top panel) Change in formation enthalpy of rhombohedral and orthorhombic Bi_2Se_3 vs. substrate lattice parameter for various epitaxial relations with the cubic BiSe (001) surface. Low-index surfaces have been considered for epitaxy on BiSe, including the (001) surface of rhombohedral Bi_2Se_3, and the (010), (100), (001), and (201) surfaces of orthorhombic Bi_2Se_3 (bottom panel). The experimental and DFT-calculated lattice parameters of the cubic BiSe substrate are 5.73 Å (obtained from **Figure 6b**) and 6.07 Å, respectively, which are marked with black arrows. The blue and red shaded areas indicate the regions where orthorhombic Bi_2Se_3 with the (010) and (001) surfaces have the lowest formation energy, respectively. The corresponding atomic structures of the various growth surfaces are shown in the bottom panel.

Based upon our combined experimental and computational results, we propose the following mechanism for the formation of metastable orthorhombic Bi_2Se_3, which is depicted using a schema in **Figure 9**. During the initial stage of growth, the electrochemical potential drives the deposition of hemispherical microscale particles of bismuth and selenium that are amorphous. TEM imaging reveals that cubic BiSe nanocrystals precipitate within this amorphous seed layer. The initial seed layer is rich in Bi relative to the stoichiometry of Bi_2Se_3 (see **Figure 4**), but the films become richer in Se over time. As the stoichiometry of the film approaches that of Bi_2Se_3, crystallites of Bi_2Se_3 nucleate from the seed layer. DFT calculations indicate that the better epitaxial match between cubic BiSe and orthorhombic Bi_2Se_3 stabilizes the metastable phase. The orthorhombic Bi_2Se_3 crystallites continue to grow along the [010] direction to form platelet crystals. The occurrence of twin boundaries — that are low energy interfaces — between the different Bi_2Se_3 crystallites, as observed in our TEM experiments, results in the formation of interleaved platelets as observed by SEM (**Figures 3, 4**). This mechanism is consistent with all our experimental

observations as well as with previous reports of the conditions needed to electrodeposit orthorhombic Bi_2Se_3.[23, 25]

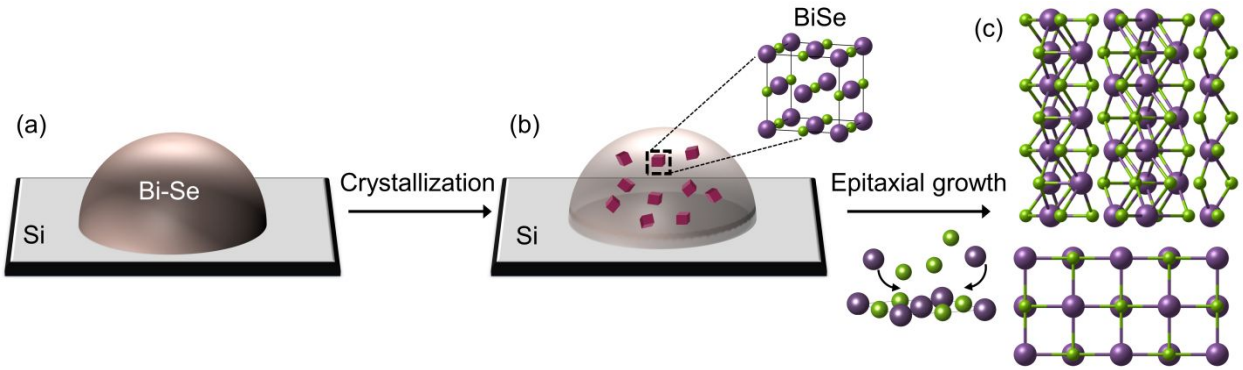

Figure 9. Schematic of the growth mechanism of metastable, orthorhombic Bi_2Se_3. (a) A Bi-rich, amorphous seed layer of Bi and Se initially deposits on the Si substrate. (b) Nanocrystals of cubic BiSe nucleate within the seed layer. (c) As the composition of the film becomes richer in Se, epitaxy between cubic BiSe and orthorhombic Bi_2Se_3 leads to the nucleation and growth of the metastable phase.

The formation of rock salt BiSe is uncommon. While we could only find one report of growing pure rock salt BiSe,[64] as a structural motif rock salt BiSe is also found in layered superstructures such as $[(BiSe)_{1+\delta}]_m[TiSe_2]_m$.[65-66] Thus, the question arises as to why this compound forms during the early stages of electrodeposition. The applied potential used to grow all Bi_2Se_3 films with the orthorhombic phase was positive of the potential needed to deposit Se directly on the Si substrate (**Figure S8**), such that only Bi is initially deposited. The deposition of Bi on the Si substrate then reduces the overpotential needed to deposit Se.[23] The reduction of $Bi(NO_3)_3$ and the lower Se:Bi ratio initially favor formation of a bismuth selenide compound in which Bi is in a lower oxidation state, such as BiSe. The increase in Se:Bi ratio with deposition time can then promote formation

of a compound in which Bi is in a higher oxidation state (i.e., Bi_2Se_3). Furthermore, the rock salt structure of BiSe is thermodynamically less stable compared to its trigonal phase. Our calculations indicate that the rock salt phase is stabilized over the trigonal phase for small crystal sizes (i.e., < 1.5 nm) due to the lower surface energies of the facets that make up the BiSe crystals (see **Supporting Discussion S4**, **Table S7**, and **Figure S21d**).

To demonstrate the generality of this seeded growth mechanism, we electrodeposited orthorhombic Bi_2Se_3 on polycrystalline substrates including fluorine-doped tin oxide (FTO) and gold. We first determined the appropriate potentials to deposit the orthorhombic phase on each substrate by performing cyclic voltammetry. Based on the potential-dependent structures of Bi_2Se_3 films grown on single-crystal Si substrates, we hypothesized that the orthorhombic phase would form at a potential positive of the Bi^{3+} reduction peak on these polycrystalline substrates. For both the FTO and Au substrates, an applied potential of 0.00 V vs. Ag/AgCl is positive of the reduction peak of $Bi(NO_3)_3$ (**Figure S22**). XRD patterns of Bi_2Se_3 films grown at this potential for a total charge density of 2 C/cm^2 are shown in **Figure 10a**. In both cases, we observe the orthorhombic phase of Bi_2Se_3. The morphology of the orthorhombic crystallites is similar to films deposited on single-crystal Si substrates. For FTO substrates, both the hemispherical seed layer and interleaved platelet microcrystals are observed (**Figure 10b, d**). On Au substrates, the seed layer is denser compared to deposition on Si and FTO substrates, and the orthorhombic Bi_2Se_3 crystallites that grow from this continuous layer have a smaller size for the same amount of material deposited (**Figure 10c, e**). The transition from island growth of the seed layer on Si and FTO to a smoother layer on Au is consistent with the higher surface energy of Au in which adatom–substrate interactions become stronger.[67] These results demonstrate that the spontaneous formation of the

seed layer enables electrodeposition of the metastable, orthorhombic phase on a variety of substrates without the requirement for a single crystal.

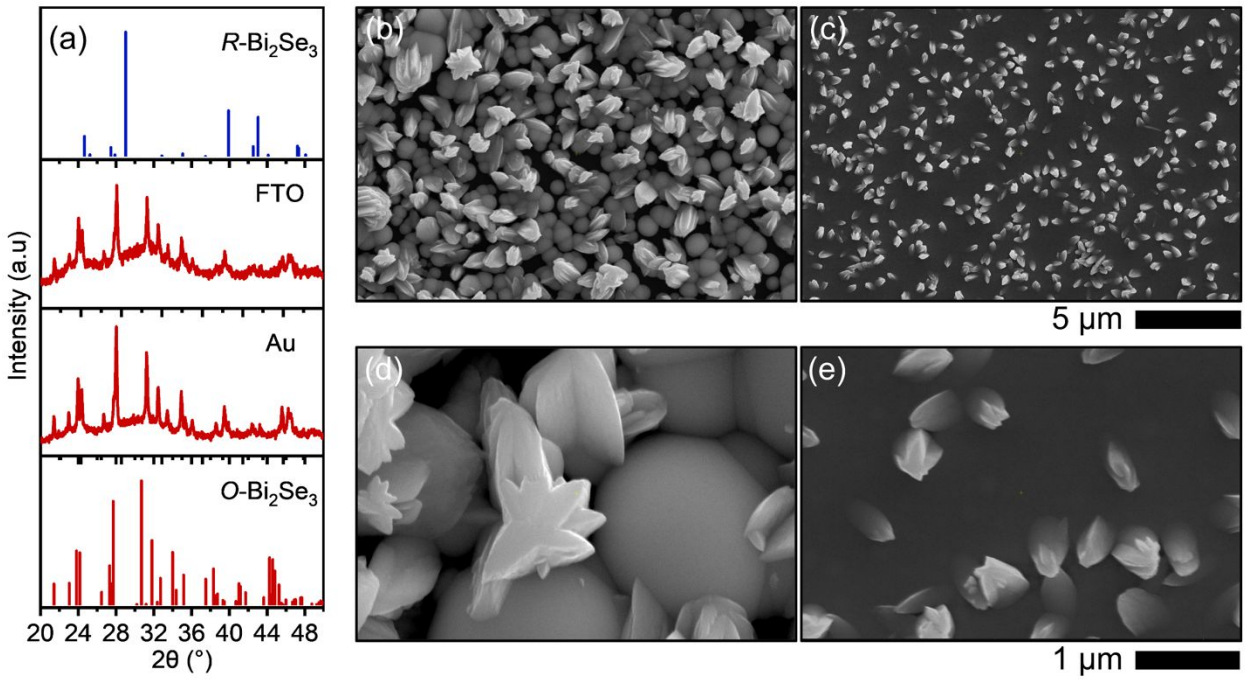

Figure 10. (a) Powder XRD patterns of Bi_2Se_3 films grown on polycrystalline FTO and Au substrates. The applied potential used to grow the films was 0.00 V vs. Ag/AgCl, and the total amount of charge passed for each film was 2 C/cm^2. (b, d) SEM images of a Bi_2Se_3 film grown on FTO. (c, e) SEM images of a Bi_2Se_3 film grown on Au. The scale bars of 5 μm and 1 μm apply to all images in the top row and bottom row, respectively.

Conclusions

In summary, by identifying the conditions needed to form the metastable phase of Bi_2Se_3 on single-crystal Si substrates, we were able to extend this growth mechanism to polycrystalline substrates including FTO-coated glass and Au. By electrodepositing the films at a potential close to or positive of the peak for Bi^{3+} reduction (which varies for different substrates), a seed layer is

produced that leads to Bi_2Se_3 films with high crystallinity and the metastable, orthorhombic phase. Electron diffraction reveals that the seed layer contains nanocrystals of cubic BiSe. DFT calculations indicate that nucleation of the orthorhombic Bi_2Se_3 microcrystals takes place on the cubic BiSe nanocrystals due to epitaxial matching between the two crystals. We hypothesize that seeded electrochemical growth using nanoscale seed particles can be used to synthesize other metastable phases of metal chalcogenide and oxide semiconductors. Targets of interest include the metastable π phase of SnS,[68-69] which is a chiral semiconductor, the metastable ε phase of Ga_2O_3,[63] a ferroelectric semiconductor, and the metastable ε phase of Fe_2O_3, a multiferroic material.[70] The ability to produce semiconductor films with metastable crystal structures by electrodeposition at room temperature without the need for a single-crystal growth substrate can facilitate the incorporation of these materials into devices for energy and information conversion and storage.

Experimental section

Materials. All chemicals were used as received. Bismuth (III) nitrate hydrate ($Bi(NO_3)_3$•xH_2O 98%), selenium dioxide (SeO_2, 99.4%), platinum gauze (Pt, 100 mesh, 99.9% metals basis), and Pt wire (0.5 mm diameter, 99.95% metals basis) were purchased from Alfa Aesar. Nitric acid (HNO_3, ≥ 97%), isopropanol (≥ 99.7%), gallium (99.999%), indium beads (99.999%) and sodium chloride (NaCl, ≥99%) were purchased from Sigma-Aldrich/Millipore Sigma. All aqueous solutions were prepared using deionized water from a GenPure Pro water purification system with a resistivity of 18.2 MΩ×cm. Single-crystal, n-type Si wafers with either the (100) or (111) orientation and varying resistivities were purchased from University Wafer, Inc., Addison Engineering, Inc., and MTI corporation (see **Table S1** in the **Supporting Information** for further details). FTO-coated glass slides with lateral dimensions of 1” × 1”, a thickness of 2.2 mm, and a

sheet resistivity of 12 – 14 Ohm/square were purchased from MTI corporation. Chrome-plated tungsten rods and Au pellets (99.999%) were purchased from the Kurt J. Lesker Company. Hydrofluoric acid (49%, LM grade) was purchased from the Transene Company, Inc. Hysol 9460 epoxy was purchased from McMaster-Carr. Silver conductive paint was purchased from SPI Supplies. Acetone (≥ 99.5%) was purchased from Fisher Scientific International, Inc. A eutectic liquid alloy of gallium and indium (Ga−In) was either purchased directly from VWR International, Inc. or prepared by combining the two metals in a weight ratio of approximately 75% Ga and 25% In.

Preparation of electrodes. The counter electrode used in all electrochemical experiments consisted of Pt gauze connected to a Pt wire. The Pt wire was soldered to a tinned copper wire, and the soldered joint was sealed in a glass tube. All potentials reported in this manuscript are referenced to a silver/silver chloride (Ag/AgCl) electrode in 3 M NaCl. The working electrodes consisted of single-crystal Si wafers with different orientations and resistivities (see **Table S1** in the **Supporting Information**). The Si wafers were first cut into square pieces with approximate edge lengths of either 5 or 25 mm using a diamond scribe. The larger substrates were used to measure the resistivity of the substrate and to prepare samples for characterization by powder XRD. The smaller substrates were used for all other characterization methods (e.g., thin-film XRD, SEM, TEM, XPS, and CV). To prepare each working electrode, Ga−In eutectic was scratched into the unpolished back side of the Si substrate. A coiled Cu wire was then pressed into the Ga−In liquid on the back side of the Si and coated with conductive Ag paint to seal the wire onto the substrate. Following attachment of the Si substrate, the wire was threaded through a glass tube, and Hysol 9460 epoxy was used to seal the opening of the tube. To cure the epoxy, the electrode was dried

in an oven at 60°C. Finally, nail polish was used to coat the unpolished back side of the Si electrode and the exposed portion of the Cu wire so that the Bi_2Se_3 film would only grow on the polished side of the Si substrate.

Polycrystalline Au and FTO films on glass slides were also used as working electrodes to grow Bi_2Se_3 films. An Edwards Auto 306 Vacuum Coater was used to deposit the Au films. A 10-nm adhesion layer of Cr was first deposited on the glass slide at a current of 4.2 A followed by a 100-nm film of Au at a current of 4 A. The pressure during thermal evaporation was 10^{-6} torr. The Au and FTO substrates were rinsed with deionized water and dried using a stream of nitrogen prior to use. For both Au and FTO substrates, a metal alligator clip was used to connect the substrates to the potentiostat.

Electrochemical synthesis of Bi_2Se_3 films. Bi_2Se_3 films were electrodeposited using a three-electrode configuration at a constant potential with all three electrodes in the same cell. The deposition procedure was adapted from previous reports.[23-25] The deposition solution contained 1 mM $Bi(NO_3)_3$, 1.5 mM SeO_2, and 0.5 M HNO_3. The electrochemical cell was open to air during deposition. A BioLogic VSP-300 potentiostat/galvanostat was used to perform all electrochemical experiments. Immediately before each deposition, the polished side of the Si electrode was etched by immersing it in an aqueous solution of 10% HF for 30 s to remove the native oxide layer. The electrode was then rinsed with deionized water and dried under a stream of nitrogen. An image of each electrode was taken using a photo scanner, and the electrode area was measured using ImageJ software. The electrode area was used to determine the total charge density passed between the working and counter electrodes during each deposition. The applied potential and the amount of charge passed were varied for different substrates as described in the manuscript and summarized

in **Table S2**. After each deposition, the electrode was washed with deionized water and immersed in acetone to dissolve the nail polish and Ag paint. In some cases, a small amount of Ag redeposited on the top of the electrode, leading to an impurity observed in the XRD pattern. Once the Si substrate detached from the wire, it was rinsed with DI water, and dried using a stream of nitrogen before further characterization.

Characterization.

A four-point probe (Keithley 2450 sourcemeter) was used to measure the sheet resistance of the Si substrates without the contact resistance of the native oxide layer. The distance between each probe was 1.27 mm. Each Si wafer was first cut into a square piece with dimensions of approximately 25 mm × 25 mm, and the exact edge lengths were measured. Source currents ranging from 1 μA to 5 mA were tested. We found that 100 μA was the optimal source current for Si substrates with a resistivity range of 0.001 to 0.006 Ω×cm, while 1 mA was the optimal source current for Si substrates with a resistivity range of 0.5 to 5 Ω×cm. The sheet resistivity was obtained by multiplying the sheet resistance by the thickness of the Si wafer. For each Si wafer, four measurements were taken on different areas of the substrate, and the values were averaged to determine the reported resistivity. The resistivities of Au and FTO substrates were measured through the same method as used for Si substrates. The source current was 1 mA for Au and 10 mA for FTO.

Cyclic voltammetry (CV) was performed to characterize the potentials for redox reactions to occur on different substrates (e.g., single-crystal Si, FTO-coated glass, and polycrystalline Au). All CV scans started at the open-circuit potential of the electrochemical cell. For each scan, the potential was first swept from the open-circuit potential to 0 V vs. Ag/AgCl, then swept in the

negative direction to −0.8 V, and finally swept back to 0 V, with a scan rate of 20 mV/s. For each substrate, CV scans were performed in both an aqueous solution of 1 mM $Bi(NO_3)_3$ and 0.5 M HNO_3 as well as a solution of 1.5 mM SeO_2 and 0.5 M HNO_3.

The crystalline phase of each sample was characterized by either powder x-ray diffraction (XRD) in which the film was scraped off from the growth substrate or by thin-film XRD in which the sample was left on the Si substrate. To prepare samples for powder XRD, the Bi_2Se_3 film was scraped off using a razor blade, and the powder was redispersed in isopropanol to make a suspension. The suspension was then drop cast onto a zero-background, silicon diffraction plate (MTI Corporation) and left to dry in ambient air. A Bruker D8 Advance x-ray diffractometer (Cu Kα = 0.15418 nm) was used for powder measurements. The scan range was from 10° to 60° in 2θ, the step size was 0.035° in 2θ, and the scan rate was 0.4 s per step. Grazing-incidence XRD patterns of the Bi_2Se_3 films still on the Si substrates were obtained with a Philips X'Pert diffractometer using Cu Kα source radiation with an x-ray mirror (PW3088/60) as the incident beam module and a 0.18° parallel plate collimator as the diffracted beam module. A fixed incident angle of 1° was maintained, and the instrument was operated in continuous mode with a step size of 0.03° and a counting time of 2 s.

The morphologies of the Bi_2Se_3 films were characterized using a Thermo Scientific Quattro S environmental scanning electron microscope (SEM) operating at an acceleration voltage of 20 kV. For top-down images of the films, the Si substrate was detached from the Cu wire as described above and then affixed to the SEM sample chuck using double-sided Cu tape. An Oxford AzTec energy dispersive x-ray (EDX) spectrometer was used to measure the elemental ratio of selenium and bismuth in each film. EDX spectroscopy was performed at an acceleration voltage of 20 kV. For the cross-sectional SEM images, the Si substrate was first cut in half using a diamond scribe.

The back side of the Si substrate was affixed to a vertical sample chuck using Cu tape such that the cross-section faced up towards the electron beam.

A Thermo Scientific Scios 2 Lo Vac Dual Beam FIB-SEM was used to prepare a sample for cross-sectional TEM and electron diffraction. A layer of Pt (~2 microns) was first deposited on the region of interest. Then a cross section of the Bi_2Se_3 film was cut into a lamella using a 30-kV Ga-ion beam. The lamella was then attached to a FIB TEM grid in the FIB chamber and polished down to electron transparency using the Ga-ion beam in steps of 30 kV, 16 kV, 8 kV, 5 kV and 2 kV. The cross-section foil was characterized by transmission electron microscopy using a JEOL JEM-2100F field-emission scanning transmission electron microscope operated at an accelerating voltage of 200 kV. To prepare the powder sample for electron diffraction, the Bi_2Se_3 film was scraped off from the Si substrate and dispersed in approximately 1 mL of isopropanol using sonication for 10 s. One drop of the suspension was drop cast onto a copper TEM grid and allowed to dry at room temperature. To obtain electron diffraction patterns, the samples were tilted to be parallel to the electron beam under the guidance of a Kikuchi pattern. By choosing the high-symmetry orientation of the Kikuchi pattern, the electron diffraction pattern was produced along the specific zone axis. We determined the zone axis of the obtained electron diffraction pattern by comparing it with a simulated diffraction pattern. Dark-field images were recorded by selecting the diffraction spots formed on the back focal plane of the objective lens using the smallest objective-lens aperture.

To prepare each sample for x-ray photoelectron spectroscopy (XPS), the Si substrate with Bi_2Se_3 film was cut into a smaller piece of approximately 2 mm × 2 mm. XPS was performed using a Physical Electronics 5000 Versa Probe II Scanning ESCA (XPS) Microprobe system with a base pressure below 10^{-8} Pa. XPS data were acquired using the 1486.6 eV line from a

monochromatic Al Kα source with a spherical capacitor analyzer set to a pass energy of 23.5 eV for the high-resolution scans. The beam size was 100 μm in diameter, the beam power was 25 W, and the acceleration voltage was 15 kV. The step size was 0.05 eV, and the number of sweeps was 20 cycles for carbon and 30 cycles for all other elements. To remove the oxide layer that forms on the surface of the films when left out in air, each sample was first pre-sputtered by sweeping the surface of the film with an Ar-ion beam at an acceleration voltage of 2 kV and a current of 1 μA for 2 min. All spectra were charge corrected using the carbon peak (284.6 eV). The deconvolution of peaks in the spectra were fit by using XPSPEAK software with a Shirley background. The areas of peaks during the deconvolution were constrained to be close to the expected area ratio based on the degeneracy of each spin state.

Calculation methods

Density-functional-theory (DFT) calculations were performed using the Vienna Ab Initio Simulation Package (VASP)[71] with the projector augmented-wave potentials (PAW).[72] We used the Perdew−Burke−Ernzerhof functional revised for solids (PBEsol)[73] to describe the exchange-correlation interactions. A plane-wave basis with cutoff energy of 520 eV and force tolerance criterion of 0.01 eV/Å on each atom was used. Initial structures of orthorhombic and rhombohedral Bi_2Se_3 and rock salt and trigonal BiSe (**Figure S16**) were downloaded from the ICSD. We used Γ-centered Monkhorst-Pack *k*-point meshes to sample the Brillouin zone.[74] The number of *k*-points along direction *i* was varied such that $k_i \times a_i$, where a_i is the lattice parameter along direction *i*, was ~30 for geometry optimization and ~60 for the static calculations. For the strain calculations, supercells of Bi_2Se_3 were constructed with different orientations while keeping the stoichiometry of Bi:Se to 2:3. Then, the *a* and *b* lattice parameters of the supercell were changed to match with

the smallest repeating unit of the theoretical cubic BiSe (100) surface (a_{sub}= 6.07 Å). We used the equation below to calculate the formation enthalpy (δH) of the rhombohedral and orthorhombic Bi_2Se_3 supercells with epitaxially constrained lattice parameters:

$$\delta H = E(Bi_{2n}Se_{3n}) - (2n \times E(Bi) + 3n \times E(Se)).$$

Here, $E(Bi_{2n}Se_{3n})$ is the total energy of the $Bi_{2n}Se_{3n}$ supercell with different orientations. E (Bi) and E(Se) are, respectively, the energy of one Bi atom in its stable trigonal phase and one Se atom in its stable monoclinic phase.

For the coincident site lattice calculations, the lattice parameters of the Bi_2Se_3 supercells were adjusted to perfectly match with the cubic BiSe (001) substrate. For example, as shown in **Figure S19**, orthorhombic Bi_2Se_3 with the (010) surface is matched with the cubic BiSe (001) surface. To perfectly match with the lattice parameter a_{sub} of the substrate (the relationship between a_{unit} and a_{sub} is shown in **Figure S16b**), we apply a strain δ to axes $a_{[001]}$ and $a_{[100]}$ of Bi_2Se_3 such that:

$$a_{[001]} + \delta_{[001]} = 2\sqrt{2}a_{unit} = 2a_{sub}$$

$$a_{[100]} + \delta_{[100]} = 2\sqrt{2}a_{unit} = 2a_{sub}$$

Since the experimental lattice parameter of the cubic BiSe nanocrystals is expected to vary over a range of values, we applied a variance δ_{sub} to the calculated lattice parameter of cubic BiSe. Thus, the lengths along the [001] and [100] dimensions of Bi_2Se_3 are changed as follows:

$$a_{[001]} + \delta_{[001]} = 2(a_{sub} + \delta_{sub})$$

$$a_{[100]} + \delta_{[100]} = 2(a_{sub} + \delta_{sub})$$

The strains applied along each direction of orthorhombic Bi_2Se_3 are:

$$\delta_{[001]} = 2(a_{sub} + \delta_{sub}) - a_{[001]}$$

$$\delta_{[100]} = 2(a_{sub} + \delta_{sub}) - a_{[100]}$$

Thus, the formation energy of orthorhombic Bi_2Se_3 with the (010) surface is changed according to the strain applied along each dimension.

Bader charge analysis for a series of bismuth selenide and bismuth oxide compounds was performed using the method developed by Tang *et al*.[75] The Bader charges of Bi, Se, and O in the different compounds listed in **Table S4** were obtained by subtracting the number of valence electrons of an atom within the PAW potential from the number of electrons assigned to the corresponding atom after the charge density partition. If the difference in Bader charge for atoms of a species was greater than 0.1, we classified them into separate groups. The Bader charge was averaged among atoms within the same group.

To determine the relative stabilities of cubic and trigonal BiSe nanocrystals as a function of size, we first computed the energies of various low-index surfaces of cubic and trigonal BiSe using slab models having a vacuum region of at least 15 Å in thickness. These slabs have symmetric top and bottom surfaces (see the Data Availability Statement below for a link that provides the slab models). The calculated surface energies were used within the WulffPack program[76] to create equilibrium crystal morphologies, as shown in **Figure S21a** and **b**. To compare the energies of cubic and trigonal BiSe nanocrystals — that have different shapes and numbers of atoms — as a function of their size, we calculated the Gibbs formation energy, $E(R)$, using the formula shown below:[77]

$$E(R) = E_{\text{Bulk}} + (\frac{1}{\text{R}})\eta\rho\gamma,$$

where E_{Bulk} is the bulk formation energy per BiSe unit (eV/BiSe) — it is the same as the formation enthalpy, as we ignore the entropic and zero-point energy contributions to the free energy, R is the "effective radius" of the nanocrystal, η is a unitless shape factor used to compare nanocrystals of different shapes,[78] ρ is the density of the BiSe nanocrystal, which is the total volume normalized

per BiSe formula unit (Å^3/BiSe), and γ is the surface energy averaged over the nanocrystal (eV/Å^2). The computed values of E_{Bulk}, η, ρ, and γ are shown in the **Table S7**. The shape factor $\eta = S/V^{2/3}$, where S is the total surface area and V is the volume of the equilibrium morphology. Different equilibrium morphologies have their own shape factor.[77] We plotted the total surface area as a function of the volume$^{2/3}$ for the equilibrium morphologies of cubic and trigonal BiSe (see **Figure 21c**), and the slope of each trace gives the shape factor.

Supporting Information Available:

Supporting discussion of Bader charge analysis of bismuth selenide and oxide compounds; the search process used to find Bi–Se compounds in the ISCD and identify the structure of seed layer; the formation enthalpy of orthorhombic and rhombohedral Bi_2Se_3 when interfaced with the (110) surface of cubic BiSe; size dependence of the relative stabilities of cubic and trigonal BiSe nanocrystals. Supporting tables providing the orientation, resistivity, and thickness of the Si substrates used to grow Bi_2Se_3 films, the electrodeposition parameters used to grow Bi_2Se_3 films, binding energies for Bi 4f x-ray photoelectron peaks after deconvolution of the spectra into contributions from different oxidation states, the Bader charge of Bi, Se, and O in bismuth selenide and oxide compounds, a summary of the structures of compounds containing Bi and Se from the ICSD, calculated surface energies of cubic BiSe, trigonal BiSe, orthorhombic Bi_2Se_3, and rhombohedral Bi_2Se_3, calculated average surface energy, shape factor, volume per BiSe unit, and bulk formation enthalpy for cubic and trigonal BiSe; Supporting figures showing current traces during the electrodeposition of the Bi_2Se_3 films, powder XRD patterns of Bi_2Se_3 films grown on Si substrates with different orientations and resistivities, cyclic voltammograms in a solution of SeO_2 and HNO_3 using different Si substrates as the working electrode, SEM image and thin-film

XRD pattern of the seed layer formed during the initial growth stage, SEM images of rhombohedral Bi_2Se_3 films grown for different charge densities, additional XPS results for Bi_2Se_3 films with the orthorhombic and rhombohedral structures, plots of the Bader charge of Bi in different bismuth selenide and oxide compounds, the unit cells of cubic and trigonal BiSe and the smallest repeating unit on the cubic BiSe (001) surface, a simulated electron diffraction pattern of Bi_2Se_3 with the Zn_3P_2 structure, additional cross-sectional TEM images and electron diffraction patterns of a Bi_2Se_3 film, coincident site lattice models for different surfaces of rhombohedral and orthorhombic Bi_2Se_3 matched with the cubic BiSe (001) surface, change in the formation enthalpy of rhombohedral and orthorhombic Bi_2Se_3 matched with the cubic BiSe (110) surface as a function of the substrate lattice parameter, the equilibrium morphologies and Gibbs formation energy of cubic and trigonal BiSe nanocrystals, cyclic voltammograms in a solution of $Bi(NO_3)_3$ and HNO_3 using Au and FTO substrates as the working electrode.

Data Availability Statement.

The data underlying this study are openly available in Zenodo at https://zenodo.org/record/6987295#.Yvqd4-zMIXp

Acknowledgements.

This material is based upon work supported by the National Science Foundation (NSF) under grant no. CHE-1753344 to B.S.; and CBET-1729787, DMR-1806147 and DMR-2122070 to R.M. Electron microscopy, focused ion-beam milling, and x-ray photoelectron spectroscopy were performed at the Institute of Materials Science & Engineering at Washington University. Powder x-ray diffraction was performed in the Department of Earth and Planetary Sciences at Washington

University. Thin-film XRD was performed at the Advanced Materials Characterization Laboratory at the Missouri University of Science and Technology. B.M.C. acknowledges support from the MARC U-STAR program at Washington University. The authors thank J. D'Arcy and Y. Lu for use of their 4-point probe apparatus.

References

1. Wang, Z.; Hou, J.; Yang, C.; Jiao, S.; Huang, K.; Zhu, H., Hierarchical Metastable γ-TaON Hollow Structures for Efficient Visible-Light Water Splitting. *Energy & Environmental Science* **2013,** *6*, 2134-2144.
2. Shao, Q.; Wang, Y.; Yang, S.; Lu, K.; Zhang, Y.; Tang, C.; Song, J.; Feng, Y.; Xiong, L.; Peng, Y.; Li, Y.; Xin, H. L.; Huang, X., Stabilizing and Activating Metastable Nickel Nanocrystals for Highly Efficient Hydrogen Evolution Electrocatalysis. *ACS Nano* **2018,** *12*, 11625-11631.
3. Wang, Y.; Sun, D.; Chowdhury, T.; Wagner, J. S.; Kempa, T. J.; Hall, A. S., Rapid Room-Temperature Synthesis of a Metastable Ordered Intermetallic Electrocatalyst. *Journal of the American Chemical Society* **2019,** *141*, 2342-2347.
4. Duan, Y.; Sun, S.; Sun, Y.; Xi, S.; Chi, X.; Zhang, Q.; Ren, X.; Wang, J.; Ong, S. J. H.; Du, Y.; Gu, L.; Grimaud, A.; Xu, Z. J., Mastering Surface Reconstruction of Metastable Spinel Oxides for Better Water Oxidation. *Advanced Materials* **2019,** *31*, 1807898.
5. Zhang, S.; Huang, Z.; Wen, Z.; Zhang, L.; Jin, J.; Shahbazian-Yassar, R.; Yang, J., Local Lattice Distortion Activate Metastable Metal Sulfide as Catalyst with Stable Full Discharge–Charge Capability for Li–O_2 Batteries. *Nano Letters* **2017,** *17*, 3518-3526.
6. Higgins, D.; Wette, M.; Gibbons, B. M.; Siahrostami, S.; Hahn, C.; Escudero-Escribano, M.; García-Melchor, M.; Ulissi, Z.; Davis, R. C.; Mehta, A.; Clemens, B. M.; Nørskov, J. K.; Jaramillo, T. F., Copper Silver Thin Films with Metastable Miscibility for Oxygen Reduction Electrocatalysis in Alkaline Electrolytes. *ACS Applied Energy Materials* **2018,** *1*, 1990-1999.

7. Zu, C.; Wang, W. B.; He, L.; Zhang, W. G.; Dai, C. Y.; Wang, F.; Duan, L. M., Experimental Realization of Universal Geometric Quantum Gates with Solid-State Spins. *Nature* **2014,** *514*, 72-75.

8. Pezzagna, S.; Meijer, J., Quantum Computer Based on Color Centers in Diamond. *Applied Physics Reviews* **2021,** *8*, 011308.

9. Yan, C.-s.; Vohra, Y. K.; Mao, H.-k.; Hemley, R. J., Very High Growth Rate Chemical Vapor Deposition of Single-Crystal Diamond. *Proceedings of the National Academy of Sciences* **2002,** *99*, 12523-12525.

10. Rabeau, J. R.; Stacey, A.; Rabeau, A.; Prawer, S.; Jelezko, F.; Mirza, I.; Wrachtrup, J., Single Nitrogen Vacancy Centers in Chemical Vapor Deposited Diamond Nanocrystals. *Nano Letters* **2007,** *7*, 3433-3437.

11. Achard, J.; Jacques, V.; Tallaire, A., Chemical Vapour Deposition Diamond Single Crystals with Nitrogen-Vacancy Centres: A Review of Material Synthesis and Technology for Quantum Sensing Applications. *Journal of Physics D: Applied Physics* **2020,** *53*, 313001.

12. Kucsko, G.; Maurer, P. C.; Yao, N. Y.; Kubo, M.; Noh, H. J.; Lo, P. K.; Park, H.; Lukin, M. D., Nanometre-Scale Thermometry in a Living Cell. *Nature* **2013,** *500*, 54-58.

13. Sines, I. T.; Misra, R.; Schiffer, P.; Schaak, R. E., Colloidal Synthesis of Non-Equilibrium Wurtzite-Type MnSe. *Angewandte Chemie International Edition* **2010,** *49*, 4638-4640.

14. Bergerud, A.; Buonsanti, R.; Jordan-Sweet, J. L.; Milliron, D. J., Synthesis and Phase Stability of Metastable Bixbyite V_2O_3 Colloidal Nanocrystals. *Chemistry of Materials* **2013,** *25*, 3172-3179.

15. Martinolich, A. J.; Kurzman, J. A.; Neilson, J. R., Polymorph Selectivity of Superconducting $CuSe_2$ through Kinetic Control of Solid-State Metathesis. *Journal of the American Chemical Society* **2015,** *137*, 3827-3833.
16. Martinolich, A. J.; Kurzman, J. A.; Neilson, J. R., Circumventing Diffusion in Kinetically Controlled Solid-State Metathesis Reactions. *Journal of the American Chemical Society* **2016,** *138*, 11031-11037.
17. Tochitskii, T. A.; Shadrow, V. G.; Nemtsevich, L. V.; Boltushkin, A. V., On the Mechanism of Metastable Phases' Formation in Electrodeposited Co-Based Films. *Crystal Research and Technology* **1996,** *31*, 583-588.
18. Cavallotti, P. L.; Nobili, L.; Vicenzo, A., Phase Structure of Electrodeposited Alloys. *Electrochimica Acta* **2005,** *50*, 4557-4565.
19. Wang, T.; Li, F.; Wang, Y.; Song, L., Structure and Magnetic Properties of Metastable Co–Cu Solid Solution Nanowire Arrays Fabricated by Electrodeposition. *physica status solidi (a)* **2006,** *203*, 2426-2431.
20. Crozier, B.; Liu, Q.; Ivey, D. G., Formation and Transformation of Metastable Phases During Electrodeposition and Annealing of Cobalt–Iron Alloy Films. *Journal of Materials Science: Materials in Electronics* **2011,** *22*, 614-625.
21. Switzer, J. A.; Shumsky, M. G.; Bohannan, E. W., Electrodeposited Ceramic Single Crystals. *Science* **1999,** *284*, 293-296.
22. Mathe, M. K.; Cox, S. M.; Flowers, B. H.; Vaidyanathan, R.; Pham, L.; Srisook, N.; Happek, U.; Stickney, J. L., Deposition of CdSe by EC-ALE. *Journal of Crystal Growth* **2004,** *271*, 55-64.

23. Tumelero, M. A.; Benetti, L. C.; Isoppo, E.; Faccio, R.; Zangari, G.; Pasa, A. A., Electrodeposition and *ab Initio* Studies of Metastable Orthorhombic Bi_2Se_3: A Novel Semiconductor with Bandgap for Photovoltaic Applications. *The Journal of Physical Chemistry C* **2016,** *120*, 11797-11806.

24. Souza, P. B.; Tumelero, M. A.; Zangari, G.; Pasa, A. A., Tuning Electrodeposition Conditions Towards the Formation of Smooth Bi_2Se_3 Thin Films. *Journal of The Electrochemical Society* **2017,** *164*, D401-D405.

25. Ahmed, R.; Lin, Q.; Xu, Y.; Zangari, G., Growth, Morphology and Crystal Structure of Electrodeposited Bi_2Se_3 Films: Influence of the Substrate. *Electrochimica Acta* **2019,** *299*, 654-662.

26. Sorenson, T. A.; Morton, S. A.; Waddill, G. D.; Switzer, J. A., Epitaxial Electrodeposition of Fe_3O_4 Thin Films on the Low-Index Planes of Gold. *Journal of the American Chemical Society* **2002,** *124*, 7604-7609.

27. Villegas, I.; Stickney, J. L., Preliminary Studies of GaAs Deposition on Au(100), (110), and (111) Surfaces by Electrochemical Atomic Layer Epitaxy. *Journal of The Electrochemical Society* **1992,** *139*, 686-694.

28. Golden, T. D.; Shumsky, M. G.; Zhou, Y.; VanderWerf, R. A.; Van Leeuwen, R. A.; Switzer, J. A., Electrochemical Deposition of Copper(I) Oxide Films. *Chemistry of Materials* **1996,** *8*, 2499-2504.

29. Carim, A. I.; Collins, S. M.; Foley, J. M.; Maldonado, S., Benchtop Electrochemical Liquid–Liquid–Solid Growth of Nanostructured Crystalline Germanium. *Journal of the American Chemical Society* **2011,** *133*, 13292-13295.

30. Fahrenkrug, E.; Gu, J.; Maldonado, S., Electrodeposition of Crystalline GaAs on Liquid Gallium Electrodes in Aqueous Electrolytes. *Journal of the American Chemical Society* **2013,** *135*, 330-339.

31. Kim, T. W.; Woo, M. A.; Regis, M.; Choi, K.-S., Electrochemical Synthesis of Spinel Type $ZnCo_2O_4$ Electrodes for Use as Oxygen Evolution Reaction Catalysts. *The Journal of Physical Chemistry Letters* **2014,** *5*, 2370-2374.

32. Lowe, James M.; Yan, Q.; Benamara, M.; Coridan, R. H., Direct Photolithographic Patterning of Cuprous Oxide Thin Films Via Photoelectrodeposition. *Journal of Materials Chemistry A* **2017,** *5*, 21765-21772.

33. Wheeler, G. P.; Choi, K.-S., Photoelectrochemical Properties and Stability of Nanoporous p-Type $LaFeO_3$ Photoelectrodes Prepared by Electrodeposition. *ACS Energy Letters* **2017,** *2*, 2378-2382.

34. Banik, A.; Tubbesing, J. Z.; Luo, B.; Zhang, X.; Switzer, J. A., Epitaxial Electrodeposition of Optically Transparent Hole-Conducting CuI on n-Si(111). *Chemistry of Materials* **2021,** *33*, 3220-3227.

35. Kang, D.; Kim, T. W.; Kubota, S. R.; Cardiel, A. C.; Cha, H. G.; Choi, K.-S., Electrochemical Synthesis of Photoelectrodes and Catalysts for Use in Solar Water Splitting. *Chemical Reviews* **2015,** *115*, 12839-12887.

36. Fahrenkrug, E.; Maldonado, S., Electrochemical Liquid–Liquid–Solid (ec-LLS) Crystal Growth: A Low-Temperature Strategy for Covalent Semiconductor Crystal Growth. *Accounts of Chemical Research* **2015,** *48*, 1881-1890.

37. Sarkar, D.; Wang, W.; Mecklenburg, M.; Clough, A. J.; Yeung, M.; Ren, C.; Lin, Q.; Blankemeier, L.; Niu, S.; Zhao, H.; Shi, H.; Wang, H.; Cronin, S. B.; Ravichandran, J.; Luhar,

M.; Kapadia, R., Confined Liquid-Phase Growth of Crystalline Compound Semiconductors on Any Substrate. *ACS Nano* **2018,** *12*, 5158-5167.

38. Konstantatos, G.; Levina, L.; Tang, J.; Sargent, E. H., Sensitive Solution-Processed Bi_2S_3 Nanocrystalline Photodetectors. *Nano Letters* **2008,** *8*, 4002-4006.
39. Xu, J.; Li, H.; Fang, S.; Jiang, K.; Yao, H.; Fang, F.; Chen, F.; Wang, Y.; Shi, Y., Synthesis of Bismuth Sulfide Nanobelts for High Performance Broadband Photodetectors. *Journal of Materials Chemistry C* **2020,** *8*, 2102-2108.
40. Filip, M. R.; Patrick, C. E.; Giustino, F., *GW* Quasiparticle Band Structures of Stibnite, Antimonselite, Bismuthinite, and Guanajuatite. *Physical Review B* **2013,** *87*, 205125.
41. Biswas, K.; Zhao, L.-D.; Kanatzidis, M. G., Tellurium-Free Thermoelectric: The Anisotropic *n*-Type Semiconductor Bi_2S_3. *Advanced Energy Materials* **2012,** *2*, 634-638.
42. Liu, W.; Lukas, K. C.; McEnaney, K.; Lee, S.; Zhang, Q.; Opeil, C. P.; Chen, G.; Ren, Z., Studies on the Bi_2Te_3–Bi_2Se_3–Bi_2S_3 System for Mid-Temperature Thermoelectric Energy Conversion. *Energy & Environmental Science* **2013,** *6*, 552-560.
43. Witting, I. T.; Chasapis, T. C.; Ricci, F.; Peters, M.; Heinz, N. A.; Hautier, G.; Snyder, G. J., The Thermoelectric Properties of Bismuth Telluride. *Advanced Electronic Materials* **2019,** *5*, 1800904.
44. Ahmed, R.; Rosul, M. G.; Xu, Y.; Zebarjadi, M.; Zangari, G., Morphology and Seebeck Coefficients of Electrodeposited Bi_2Se_3 Films Grown onto Au(111)/Si Substrates. *Electrochimica Acta* **2021,** *368*, 137554.
45. Zhang, H.; Liu, C.-X.; Qi, X.-L.; Dai, X.; Fang, Z.; Zhang, S.-C., Topological Insulators in Bi_2Se_3, Bi_2Te_3 and Sb_2Te_3 with a Single Dirac Cone on the Surface. *Nature Physics* **2009,** *5*, 438-442.

46. Jeong, K.; Park, H.; Chae, J.; Sim, K.-i.; Yang, W. J.; Kim, J.-h.; Hong, S.-b.; Kim, J. H.; Cho, M.-h., Topological Phase Control of Surface States in Bi_2Se_3 via Spin–Orbit Coupling Modulation through Interface Engineering between HfO_{2-X}. *ACS Applied Materials & Interfaces* **2020,** *12*, 12215-12226.

47. Tan, D.; Zhang, W.; Wang, X.; Koirala, S.; Miyauchi, Y.; Matsuda, K., Polarization-Sensitive and Broadband Germanium Sulfide Photodetectors with Excellent High-Temperature Performance. *Nanoscale* **2017,** *9*, 12425-12431.

48. Chen, S.; Cao, R.; Chen, X.; Wu, Q.; Zeng, Y.; Gao, S.; Guo, Z.; Zhao, J.; Zhang, M.; Zhang, H., Anisotropic Plasmonic Nanostructure Induced Polarization Photoresponse for MoS_2-Based Photodetector. *Advanced Materials Interfaces* **2020,** *7*, 1902179.

49. Tumelero, M. A.; Martins, M. B.; Souza, P. B.; Della Pace, R. D.; Pasa, A. A., Effect of Electrolyte on the Growth of Thermoelectric Bi_2Se_3 Thin Films. *Electrochimica Acta* **2019,** *300*, 357-362.

50. Torane, A. P.; Lokhande, C. D.; Patil, P. S.; Bhosale, C. H., Preparation and Characterization of Electrodeposited Bi_2Se_3 Thin Films. *Materials Chemistry and Physics* **1998,** *55*, 51-54.

51. Desai, J. D., Electrodeposition of Bi_2Se_3 Thin Films. *Bulletin of Electrochemistry* **1999,** *15*, 315-317.

52. Xiao, C.; Yang, J.; Zhu, W.; Peng, J.; Zhang, J., Electrodeposition and Characterization of Bi_2Se_3 Thin Films by Electrochemical Atomic Layer Epitaxy (ECALE). *Electrochimica Acta* **2009,** *54*, 6821-6826.

53. Peng, H.; Zhou, J.; Tang, D.; Lai, Y.; Liu, F.; Li, J.; Liu, Y., Preparation and Characterization of Bi_2Se_3 Nanowires by Electrodeposition. *Electrochimica Acta* **2011,** *56*, 5085-5089.

54. Li, J.; Wang, B.; Liu, F.; Liu, J.; Jia, M.; Lai, Y.; Li, J.; Liu, Y., Structural and Optical Properties of Electrodeposited $Bi_{2-X}Sb_XSe_3$ Thin Films. *ECS Solid State Letters* **2012,** *1*, Q29-Q31.

55. Han, C.; Yang, J.; Yan, C.; Li, Y.; Liu, F.; Jiang, L.; Ye, J.; Liu, Y., The Electrochemical Self-Assembly of Hierarchical Dendritic Bi_2Se_3 Nanostructures. *CrystEngComm* **2014,** *16*, 2823-2834.

56. Inorganic Crystal Structure Database https://icsd.products.fiz-karlsruhe.de/ (accessed 2022-04-01).

57. Ahmed, R.; Xu, Y.; Sales, M. G.; Lin, Q.; McDonnell, S.; Zangari, G., Synthesis and Material Properties of Bi_2Se_3 Nanostructures Deposited by SILAR. *The Journal of Physical Chemistry C* **2018,** *122*, 12052-12060.

58. Li, Y.; Cheng, J.; Song, J.; Alonso, J. A.; Fernández-Díaz, M. T.; Goodenough, J. B., Characterization of the Double Perovskite $Ba_2Bi_xSc_{0.2}Co_{1.8-x}O_{6-\delta}$ (x = 0.1, 0.2). *Chemistry of Materials* **2012,** *24*, 4114-4122.

59. Li, H.; Shang, J.; Zhu, H.; Yang, Z.; Ai, Z.; Zhang, L., Oxygen Vacancy Structure Associated Photocatalytic Water Oxidation of BiOCl. *ACS Catalysis* **2016,** *6*, 8276-8285.

60. Bhachu, D. S.; Moniz, S. J. A.; Sathasivam, S.; Scanlon, D. O.; Walsh, A.; Bawaked, S. M.; Mokhtar, M.; Obaid, A. Y.; Parkin, I. P.; Tang, J.; Carmalt, C. J., Bismuth Oxyhalides: Synthesis, Structure and Photoelectrochemical Activity. *Chemical Science* **2016,** *7*, 4832-4841.

61. Mao, C.; Cheng, H.; Tian, H.; Li, H.; Xiao, W.-J.; Xu, H.; Zhao, J.; Zhang, L., Visible Light Driven Selective Oxidation of Amines to Imines with BiOCl: Does Oxygen Vacancy Concentration Matter? *Applied Catalysis B: Environmental* **2018,** *228*, 87-96.

62. Vasileiadis, T.; Skountzos, E. N.; Foster, D.; Coleman, S. P.; Zahn, D.; Krečinić, F.; Mavrantzas, V. G.; Palmer, R. E.; Ernstorfer, R., Ultrafast Rotational Motions of Supported Nanoclusters Probed by Electron Diffraction. *Nanoscale Horizons* **2019,** *4*, 1164-1173.

63. Cho, S. B.; Mishra, R., Epitaxial Engineering of Polar ε-Ga_2O_3 for Tunable Two-Dimensional Electron Gas at the Heterointerface. *Applied Physics Letters* **2018,** *112*, 162101.

64. Semiletov, S. A., An Electron Diffraction Study of Films of Bi-Se and Bi-Te Prepared by Evaporation. *Trudy Instituta Kristallografii, Akademiya Nauk SSSR* **1954,** *10*, 76-83.

65. Trump, B. A.; Livi, K. J. T.; McQueen, T. M., The New Misfit Compound $(BiSe)_{1.15}(TiSe_2)_2$ and the Role of Dimensionality in the $Cu_x(BiSe)_{1+\delta}(TiSe_2)_n$ Series. *Journal of Solid State Chemistry* **2014,** *209*, 6-12.

66. Lygo, A. C.; Hamann, D. M.; Moore, D. B.; Merrill, D. R.; Ditto, J.; Esters, M.; Orlowicz, J.; Wood, S. R.; Johnson, D. C., Kinetically Controlled Formation and Decomposition of Metastable $[(BiSe)_{1+\delta}]_m[TiSe_2]_m$ Compounds. *Journal of the American Chemical Society* **2018,** *140*, 3385-3393.

67. Penner, R. M., Mesoscopic Metal Particles and Wires by Electrodeposition. *The Journal of Physical Chemistry B* **2002,** *106*, 3339-3353.

68. Rabkin, A.; Samuha, S.; Abutbul, R. E.; Ezersky, V.; Meshi, L.; Golan, Y., New Nanocrystalline Materials: A Previously Unknown Simple Cubic Phase in the SnS Binary System. *Nano Letters* **2015,** *15*, 2174-2179.

69. Abutbul, R. E.; Garcia-Angelmo, A. R.; Burshtein, Z.; Nair, M. T. S.; Nair, P. K.; Golan, Y., Crystal Structure of a Large Cubic Tin Monosulfide Polymorph: An Unraveled Puzzle. *CrystEngComm* **2016,** *18*, 5188-5194.

70. Yasuhara, S.; Hamasaki, Y.; Katayama, T.; Ao, T.; Inaguma, Y.; Hojo, H.; Karppinen, M.; Philip, A.; Yasui, S.; Itoh, M., Modulating the Structure and Magnetic Properties of ε-Fe_2o_3 Nanoparticles via Electrochemical Li^+ Insertion. *Inorganic Chemistry* **2020,** *59*, 4357-4365.
71. Blöchl, P. E., Projector Augmented-Wave Method. *Physical Review B* **1994,** *50*, 17953-17979.
72. Kresse, G.; Furthmüller, J., Efficient Iterative Schemes for *ab Initio* Total-Energy Calculations Using a Plane-Wave Basis Set. *Physical Review B* **1996,** *54*, 11169-11186.
73. Perdew, J. P.; Ruzsinszky, A.; Csonka, G. I.; Vydrov, O. A.; Scuseria, G. E.; Constantin, L. A.; Zhou, X.; Burke, K., Restoring the Density-Gradient Expansion for Exchange in Solids and Surfaces. *Physical Review Letters* **2008,** *100*, 136406.
74. Cen, J.; Pallikara, I.; Skelton, J. M., Structural Dynamics and Thermal Transport in Bismuth Chalcogenide Alloys. *Chemistry of Materials* **2021,** *33*, 8404-8417.
75. Tang, W.; Sanville, E.; Henkelman, G., A Grid-Based Bader Analysis Algorithm without Lattice Bias. *Journal of Physics: Condensed Matter* **2009,** *21*, 084204.
76. Magnus Rahm, J.; Erhart, P., WulffPack: A Python Package for Wulff Constructions. *Journal of Open Source Software* **2020,** *5*, 1944.
77. Sun, W.; Kitchaev, D. A.; Kramer, D.; Ceder, G., Non-Equilibrium Crystallization Pathways of Manganese Oxides in Aqueous Solution. *Nature Communications* **2019,** *10*, 573.
78. Qi, W. H.; Wang, M. P.; Liu, Q. H., Shape Factor of Nonspherical Nanoparticles. *Journal of Materials Science* **2005,** *40*, 2737-2739.

TOC graphic

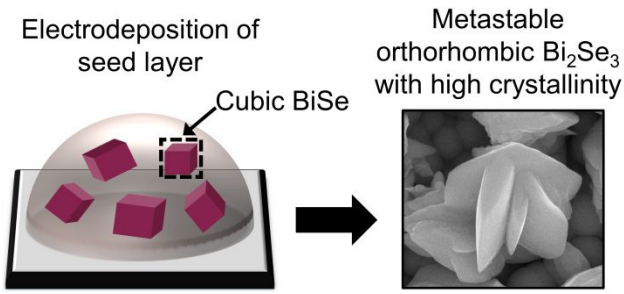
Electrodeposition of seed layer
Cubic BiSe
Metastable orthorhombic Bi_2Se_3 with high crystallinity